

# Imaging the disk-halo interface of NGC 891: a 2.7 kpc-thick molecular gas disk

D. Jiménez-López, S. García-Burillo, M. Querejeta, A. Usero, P. Tarrío

Observatorio Astronómico Nacional, Madrid, Spain

e-mail: d.jimenez@oan.es, s.gburillo@oan.es, m.querejeta@oan.es, a.usero@oan.es, p.tarrío@oan.es

## ABSTRACT

*Context.* Halos surrounding spiral galaxies act as the bridges connecting the galactic disk and the intergalactic medium (IGM). They host a significant fraction of the baryonic mass in the Universe, and feedback from star formation (SF) or active galactic nuclei (AGN) likely plays an important role in regulating this vertical baryonic component. Despite its importance, the contribution of extraplanar molecular gas remains poorly understood.

*Aims.* We aim to characterize the vertical extent and the kinematics of molecular gas traced by CO(2-1) emission in the nearby ( $D = 9.5$  Mpc) spiral galaxy NGC 891, one of the best studied edge-on galaxies. We also compare our results with the extraplanar distribution of other tracers of baryonic matter, including atomic gas (HI), diffuse ionized gas (H $\alpha$ -traced DIG), and dust maps from the literature.

*Methods.* Our analysis is based on new CO(2-1) observations of NGC 891 obtained with the IRAM 30m telescope. We mapped two 6 kpc  $\times$  6 kpc regions on the northeastern side and the area surrounding the galactic center. We apply a careful method to estimate and remove the residual contribution of the error beam to the CO cube.

*Results.* The vertical extent of the molecular gas is best described by a two-component Gaussian fit, consisting of a bright thin disk component (deconvolved  $FWHM \approx 360$  pc) and a fainter thick disk component (deconvolved  $FWHM \approx 1.1$  kpc). Statistically significant ( $> 3\sigma$ ) CO(2-1) emission is detected up to 1.3-1.4 kpc above the disk midplane. We estimate that the thick molecular disk component contains up to  $\sim 27\%$  of the total molecular gas mass of the galaxy. The vertical extent of H $\alpha$  emission is similar to that of the molecular gas, whereas HI extends much further.

*Conclusions.* Our results demonstrate that SF-driven feedback in a non-starburst galaxy can lift significant amounts of molecular gas to large vertical distances. We interpret the presence of extraplanar molecular gas in NGC 891 in the framework of a galactic fountain scenario, in which material is expelled from star-forming regions and transported toward the outer halo. This is supported by optical images where dust columns rise from the inner disk, showing spatial correlation between CO (2-1), H $\alpha$ , and dust.

**Key words.** galaxies: individual: NGC 891 – galaxies: ISM – radio lines: galaxies – galaxies: halos – galaxies: structure – galaxies: spiral

## 1. Introduction

Galaxy halos surrounding spiral galaxies connect the inner galactic disk and the circumgalactic medium (CGM). This special environment is regulated by the balance between inflow and outflow of matter and energy between these two systems. Material found in the galactic halo may come from the CGM via cooling or be ejected from the galaxy midplane by, e.g., supernova events and stellar clusters. In-depth studies of these feedback mechanisms that regulate the cycle of extraplanar baryonic matter are essential to understanding the disk-halo interaction in spiral galaxies. Ultimately, the disk-halo interaction is responsible for regulating the cycle of baryonic material and has important consequences on the star formation rate and metallicity evolution of the galaxy.

Galaxy halos, along with the CGM, host a significant fraction of the baryonic mass of the Universe (Sommer-Larsen 2006; Li et al. 2018). Previous studies suggest that the baryonic matter found in these environments may originate from outflows driven from the inner galactic disk. However, the dominant mechanisms are still uncertain. Some authors suggest that hot ionized gas is being pushed via stellar winds and supernova (SN) explosions (Shapiro & Field 1976; Bolatto et al. 2013; Roy et al. 2016). Different works try to connect star for-

mation (SF) with the distribution of hot gas (Tüllmann et al. 2006), diffuse ionized gas (DIG, Rossa & Dettmar 2003a,b; Kamphuis et al. 2007) or dust (Howk & Savage 2000). Strong outflows from active galactic nuclei (AGN) or SF can stir the interstellar medium and easily produce vertically extended components (e.g., M82, Walter et al. 2002; NGC 1068, García-Burillo et al. 2014; Mrk 231, Aalto et al. 2012, 2015; Arp 220, Barcos-Muñoz et al. 2018). This is in principle more challenging for normal, Milky Way-like galaxies, where the star formation is less intense. The processes regulating the ejection of material in those less active galaxies may take the form of galactic fountains (Bregman 1980; Melioli et al. 2008; Armillotta et al. 2016; Fraternali & Binney 2006; Li et al. 2023), whereby gas is pushed up by stellar activity, travels through the halo and eventually falls back to the disk. Recent works, such as the multiphase study of NGC 4383 by Cortese et al. (2026), provide support for galactic fountains as an important mechanism distributing material within the halo and regulating future star formation.

In recent decades, most of our knowledge about the vertical structure of gas in nearby galaxies has come from observations of the ionized component traced by H $\alpha$  (Voigtländer et al. 2013; Elliott et al. 2026), X-rays (Locatelli et al. 2024) and ra-

dio continuum (Krause et al. 2018), as well as the neutral HI gas (Heald et al. 2011) and dust (Verstappen et al. 2013). Among the different phases, the molecular gas component remains the least studied, despite its crucial role in determining the total molecular hydrogen content and indirectly controlling star formation rates. Nearby edge-on spiral galaxies are the perfect laboratory to study the cycle of matter from the disk outward to the intergalactic medium (IGM). The unique orientation of highly-inclined galaxies makes it easier to unambiguously determine the distribution of their out-of-plane gas thanks to the significant reduction of the dust extinction effects at high vertical distances and the reduction of ambiguities along the line of sight. For these reasons, many authors have chosen this kind of galaxies to study and characterize the different (out/in)flow processes and measure the vertical extent of the gas and dust. Galaxies such as NGC 5775 (Reach et al. 2025), NGC 2683 (Jiao et al. 2025), NGC 4244 (Zschaechner et al. 2011) and M82 (Wang et al. 2026) have served as case studies of the outflow mechanisms and disk-halo dynamics in edge-on galaxies.

The nearby spiral galaxy NGC 891 ( $D \approx 9.5$  Mpc, Sancisi & Allen 1979) is an excellent target for studying the disk-halo connection due to its nearly perfect edge-on inclination of  $\sim 89^\circ$  (Xilouris et al. 1998). It is similar to the Milky Way in total mass ( $M = 1.4 \times 10^{11} M_\odot$ , including dark matter; Oosterloo et al. 2007) and rotation speed ( $v_{\text{rot}}^{\text{max}} \approx 230 \text{ km s}^{-1}$ ; Swaters et al. 1997), with slightly higher star formation rate of  $\text{SFR} = 3.8 M_\odot \text{ yr}^{-1}$  (Heald et al. 2011; Evans et al. 2022). Garcia-Burillo et al. (1992) observed the CO(2-1) emission in several positions of the NGC 891 halo with the IRAM 30m telescope. They detected significant emission up to 1.3-1.6 kpc off the galaxy plane. This represented the first detection of a thick molecular disk in a non-starburst, non-active galaxy. The distribution and kinematics of the molecular gas were found to be consistent with a two-component structure consisting of a thin molecular disk 100-300 pc wide and a smoother, 2-3 kpc wide extended thick disk. The CO(1-0) map obtained with the Nobeyama 40m antenna also shows the existence of a thick molecular gas disk extending up to  $\approx 1$  kpc (Sofue & Nakai 1993). NGC 891 also hosts a spatially extended HI halo that reaches up to 14 kpc above of the galactic midplane. In the northeastern quadrant it stretches even farther, forming a filament that extends to about 22 kpc (Oosterloo et al. 2007). This halo hosts roughly 30% of the HI mass of the galaxy and shows many filamentary structures.

To study the galactic fountain process, it is necessary to examine the relationship between the molecular gas component and the DIG. It is thought that outflows originating from high star-forming regions are the engines that eject matter outward from the midplane. Many authors have studied this tracer to characterize the warm ionized medium of NGC 891 (e.g. Rand 1997 with the William Herschel Telescope, WHT), and the vertical extent and kinematics of the DIG (e.g. Kamphuis et al. 2007 with the TAURUS II imaging Fabry-Pérot spectrograph). Howk & Savage (2000) also studied the DIG in NGC 891 and its relation with the dust distribution in the galaxy. The recent work of Chastenot et al. (2024) confirmed that dust filaments connect to regions of high star formation rates in the midplane of the galaxy, lending weight to the idea that galactic winds play a key role in the cycle of baryonic matter.

The emission from the thick disk component of NGC 891 found by Garcia-Burillo et al. (1992) is significantly fainter than that of the thin disk. In order to reveal similar components in other galaxies, high-sensitivity observations would be required. The *FWHM* thickness values of the molecular gas in the Milky

Way reach only  $\sim 50$ -160 pc, increasing with galactocentric radius over 0–11 kpc (Dame et al. 2001; Nakanishi & Sofue 2006; Mertsch & Vittino 2021; Söding et al. 2025). However, the existence of a thick molecular component in our Galaxy similar to the one found in NGC 891 might have been missed by CO surveys. Patra (2020) suggested the presence of a thin-thick gas disk structure in spiral galaxies, although the authors noted that limitations in spatial resolution and the galaxy inclination constraints made it difficult to confirm this scenario. Furthermore, Pety et al. (2013) also suggested the existence of a diffuse molecular gas phase as a thick disk that extends hundreds of parsecs outside the galactic plane of M 51, but using indirect methods due to the close to face-on orientation of this galaxy. Other studies also pointed to the existence of thick molecular disks to explain the kinematics of molecular gas in different samples of nearby spiral galaxies (e.g. Bécuquet & Combes 1997; Caldú-Primo et al. 2013, 2015; Caldú-Primo & Schrubba 2016).

This work represents a follow-up project of the study of Garcia-Burillo et al. (1992). Unlike this earlier work, which relied on a limited number of vertical cuts perpendicular to the major axis to probe the vertical extent of molecular gas, our new dataset provides full coverage of two  $2.2' \times 2.2'$  (6 kpc  $\times$  6 kpc) fields around the central and northeastern regions of the galaxy. The enhanced sensitivity of the HETEROdyne Receiver Array (HERA) used in our work significantly improves the data quality and provides a more robust framework for studying the vertical extent of molecular gas in NGC 891. Furthermore, the measurements of the error beam of Kramer et al. (2013), which are used in this work to estimate its potential contribution to the observed signal, were mostly simultaneous with the CO observations. Moreover, the fact that we are fully-sampling the targeted region ensures a better characterization of the error beam contribution across most of the disk compared to the previous estimates of Garcia-Burillo et al. (1992).

The paper is structured as follows. Section 2 describes the IRAM 30m observations and the ancillary data used in this work. The formalism used to characterize the error beam contribution to the CO flux, as well as the derivation of the uncontaminated map used in this work are described in Section 3. Section 4 presents the main results, including a description of the distribution and kinematics of the extraplanar molecular gas. In addition, a comparison is made between the CO maps and the information obtained from other tracers of the ISM, which is derived from images of HI and H $\alpha$  emission, as well as from the distribution of dust in the galaxy. Section 5 discusses the implications for the origin of the extraplanar emission and the processes shaping its vertical structure. Section 6 summarizes our main conclusions.

## 2. Observations

### 2.1. CO (2-1) observations

The present study is based on observations carried out with the IRAM 30m telescope using the HERA receiver array during two observing sessions, spanning 2008-2010. We covered two adjacent  $2.2' \times 2.2'$  (6 kpc  $\times$  6 kpc) fields of the galaxy using similar instrumental setups (see Table 1). The first observing run targeted the northeastern half of the galaxy, while the second observing run focused on the region surrounding the galactic center. Either proposal was allocated 40 h of observing time each. Based on previous CO(2-1) observations of NGC 891 which detected out-of-plane emission with  $\text{SNR} \sim 3$ , we aimed for a  $\text{SNR} \sim 5$  across the expected width of the thick molecular disk. Our observations, with a beam size of  $11.2'' \times$

polarization	frequency (GHz)	$T_A^*$ (mK)	rms (mK)	$\Delta v$ (km·s <sup>-1</sup> )	map size ( $\Delta x \times \Delta y$ )	mapping mode	switching mode	pwv (mm)	T (hours)
HERA 1+2	230.128	11-600	3.5	20	2.2' × 2.2'	OTF	PSw	2	80h

**Table 1.** Setup used in the IRAM 30m telescope for the CO(2–1) observations of NGC 891.

11.2'' (516 pc×516 pc), achieved an rms noise of 3.5 mK ( $T_A^*$ ) in  $\Delta v = 20 \text{ km s}^{-1}$ -wide channels. Although the rms noise was not entirely uniform across the field, we adopted an average value representative of the northern and southern halves. During the data reduction, first-order baselines were fit and subtracted to the spectra by defining a velocity window encompassing the emission from the midplane and excluding it from the fit. The resulting data cube was re-gridded to a pixel size of 2'' along both spatial axes. All images of the galaxy presented in this work show maps that have been rotated to align the galaxy's major axis ( $PA \approx 23^\circ$ ; e.g., Garcia-Burillo et al. 1992; Scoville et al. 1993) with the adopted  $x$  axis. We used the coordinates of the dynamical center of the galaxy for the rotation:  $\alpha_{2000} = 02^{\text{h}}22^{\text{m}}33^{\text{s}}.063$ ,  $\delta_{2000} = 42^\circ20'52''.91$  (Garcia-Burillo et al. 1992; Scoville et al. 1993). Vertical offsets relative to the midplane are measured along the adopted  $z$  axis.

## 2.2. Ancillary data

This work benefits from previous studies of other ISM components in NGC 891, in particular the neutral hydrogen (HI), the ionized gas ( $H\alpha$ ) and the dust. Together, these tracers provide a comprehensive multi-phase framework against which we compare the distribution and kinematics of molecular gas presented in this paper.

### 2.2.1. WSRT HI observations

The neutral hydrogen data used in this work come from the deep observations of NGC 891 presented by Oosterloo et al. (2007). These observations are part of the HALOGAS survey (Heald et al. 2011) and were obtained with the Westerbork Synthesis Radio Telescope (WSRT). They rank among the deepest HI observations of an external galaxy to date.

The observations consisted of 20×12 h integrations in multi-array configurations, covering a bandwidth of 10 MHz over 1024 spectral channels. The final processed high-resolution cube has a spatial resolution of 22.4''×16.0'', an rms noise per channel of 0.090 mJy beam<sup>-1</sup>, and a minimum detectable column density ( $3\sigma$ ) of  $1.3 \times 10^{19} \text{ cm}^{-2}$ .

HI emission is detected up to vertical distances of  $\approx 22 \text{ kpc}$  above the disk midplane. The HI mass in the extended component represents  $\sim 30\%$  of the galaxy's total HI mass.

### 2.2.2. WIYN $H\alpha$ and BVI imaging

To trace the warm ionized medium and its morphology above the NGC 891 disk, we use the deep  $H\alpha$  and  $BVI$  broadband images presented by Howk & Savage (2000), obtained with the WIYN 3.5 m telescope. These sub-arcsecond resolution images reveal detailed diffuse and filamentary  $H\alpha$  emission and a network of dust filaments extending up to  $\approx 2 \text{ kpc}$  from the midplane.

### 2.2.3. Fabry–Pérot $H\alpha$ spectroscopy

Finally, we incorporate  $H\alpha$  Fabry–Pérot observations from Kamphuis et al. (2007) to obtain kinematic information on the

warm ionized medium and to compare the vertical extent of the  $H\alpha$  halo with that of the molecular gas. The data were obtained with the TAURUS II Fabry–Pérot interferometer on the 4.2 m William Herschel Telescope (WHT) at La Palma.

These observations provide angular and spectral resolution sufficient to resolve the velocity field of the ionized gas across the disk–halo interface.

## 3. Error beam estimation

As we aim to characterize the vertical extent of the molecular gas in NGC 891, it is of paramount importance to correct the observed signal for contributions from the IRAM 30m error beams. The telescope response to a point source is not represented by a single, ideal Gaussian profile. Instead, it includes additional broader, low-amplitude contributions which can add up to 30-40% of the total power at 1-3mm (Greve et al. 2009; Kramer et al. 2013).

Let  $T$  be the real brightness temperature distribution in the sky in a certain velocity channel. The *ideal* main beam brightness temperature ( $T_{\text{mb}}$ ) is defined as:

$$T_{\text{mb}} = G_{\text{mb}} \otimes T \quad (1)$$

where  $\otimes$  indicates convolution over the sky and  $G_{\text{mb}}$  is the Gaussian function of unit area that represents the telescope main beam. In practice, however, the *measured* main brightness temperature delivered by the telescope ( $\hat{T}_{\text{mb}}$ ) has an extra contribution from the emission captured by the broader error beams. As a result,

$$\hat{T}_{\text{mb}} = T_{\text{mb}} + Q \otimes T, \quad \text{with} \quad (2)$$

$$Q = \sum_{i=1}^3 \frac{P'_i}{B_{\text{eff}}} G_i. \quad (3)$$

Here, the  $G_i$  functions represent the three Gaussian error beams of the 30m telescope characterized by Kramer et al. (2013),  $B_{\text{eff}}$  is the main beam efficiency, and  $P'_i$  is the beam efficiency of the  $i^{\text{th}}$  beam error. For observations at 230 GHz with the 30m telescope, the  $P'/B_{\text{eff}}$  ratios are 7, 18 and 18%, respectively, meaning that their contribution can be typically neglected. However, when observing faint emission (e.g., the halo) close to an extended and brighter region (e.g., the disk), this contamination must be assessed and removed.

In this paper, we adopt the correction method devised by Garcia-Burillo et al. (1992), which we summarize below. In short, we define the following iterative approach:

$$T_{\text{mb}|N} \equiv \begin{cases} \hat{T}_{\text{mb}}, & N = 0 \\ \hat{T}_{\text{mb}} - Q \otimes T_{\text{mb}|N-1}, & \forall N > 0. \end{cases} \quad (4)$$

Here,  $T_{\text{mb}|N}$  is the  $N^{\text{th}}$  corrected main brightness temperature, with the  $0^{\text{th}}$  value corresponding to the actual measurement. It can be shown that, for  $N > 0$ ,

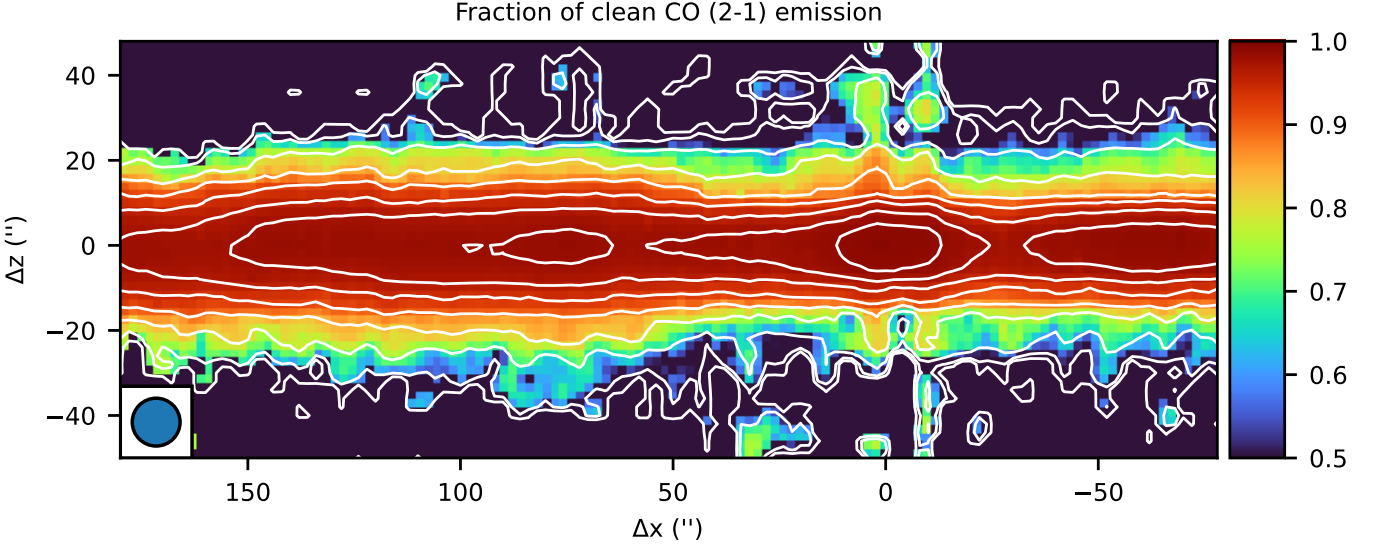


**Fig. 1.** A comparison of the observed CO integrated intensity map (in white contours: from  $3\sigma$  to  $600\sigma$ , logarithmically spaced by 0.26 dex, with  $\sigma = 0.28\text{K km s}^{-1}$ ) with the fraction of clean emission (dimensionless, in color scale) corrected for the error beam contribution, obtained after the two-step iterative process described in Sect 3. The beam size ( $11.2'' \times 11.2''$ ) is represented by the blue-filled circle at the bottom-left corner of the figure.

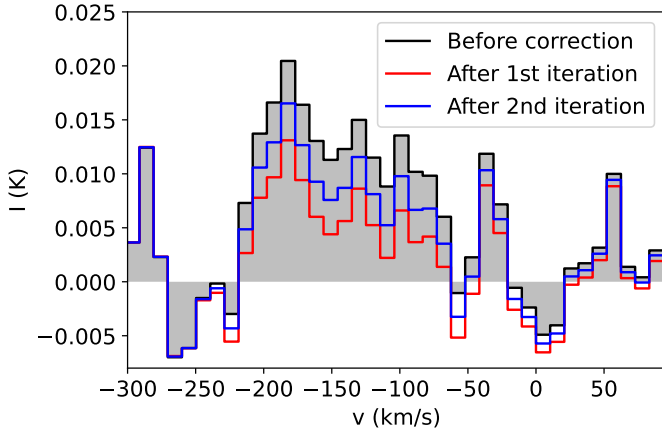


**Fig. 2.** Spectrum extracted at  $(\Delta x, \Delta z) = (75'', -30'')$ . The different curves show the initial spectrum before the correction (black) and the result obtained after the first (red curve) and second (blue curve) iteration of the error beam estimation algorithm described in Sect 3.

$$T_{\text{mb}|N} = \hat{T}_{\text{mb}} + \left( \sum_{\alpha=1}^N (-Q)^\alpha \right) \otimes \hat{T}_{\text{mb}}. \quad (5)$$

Using that  $\hat{T}_{\text{mb}} = T_{\text{mb}} + Q \otimes T$ ,

$$T_{\text{mb}|N} = T_{\text{mb}} + \left( \sum_{\alpha=1}^N (-Q)^\alpha \right) \otimes T_{\text{mb}} - \left( \sum_{\alpha=1}^{N+1} (-Q)^\alpha \right) \otimes T. \quad (6)$$

Regrouping terms, we can rewrite this as

$$T_{\text{mb}|N} = T_{\text{mb}} - (-Q)^{N+1} \otimes T_{\text{mb}} + \left( \sum_{\alpha=1}^{N+1} (-Q)^\alpha \right) \otimes (T_{\text{mb}} - T). \quad (7)$$

The equation above implies that the  $N^{\text{th}}$  corrected value is equal to the actual main brightness temperature plus two correcting terms. The first one,  $-(-Q)^{N+1} \otimes T_{\text{mb}}$ , accounts for the major contribution. This term changes its sign in each iteration and, being of order  $(P'/B_{\text{eff}})^{N+1} \ll 1$ , it becomes progressively smaller. The second term is a wavy distribution of order  $P'/B_{\text{eff}}$  with a null contribution to the area-integrated total flux. In practice, since all the error beams are much broader than the main one,  $Q \otimes T_{\text{mb}} \approx Q \otimes T$ , so this term is negligible. For the purposes of this paper, we have applied this iterative method up to  $N = 2$ , thus we consider  $T_{\text{mb}|2}$  our best estimate of the main brightness temperature corrected for error beam effects.

As the Gaussian kernels must extend over an area that goes beyond the region mapped in the observations, we first create a symmetrized mock image of the galaxy. In this image, we assign the missing pixels on the western side of the galaxy ( $x', z, v'$ ) a value of the CO flux  $T_{\text{mb}}[x' - x_c, z - z_c, v' - v_{\text{sys}}] = T_{\text{mb}}[x_c - x', z - z_c, v_{\text{sys}} - v']$ , where  $(x_c, z_c)$  and  $v_{\text{sys}}$  correspond to the coordinates of the dynamical center and the systemic velocity of the galaxy, respectively ( $v_{\text{sys}}^{\text{HEL}} = 535 \text{ km s}^{-1}$ ; Garcia-Burillo et al. 1992).

Figure 1 shows the observed CO velocity-integrated intensities ( $I_{\text{CO}}$ ) obtained by integrating the emission arising from the full velocity range due to rotation in the mapped region,  $v - v_{\text{sys}} = [-300, 300] \text{ km s}^{-1}$ , before any correction. This emission is overlaid, as white contours, on the color map of the estimated fraction of cleaned CO emission  $\frac{I_{\text{corrected}}}{I_{\text{uncorrected}}}$ , obtained after correcting for the error beam contribution using the two-step process described above. The percentage of emission free of contamination by the error beams is high ( $\geq 90\% - 95\%$ ) across the disk up to vertical distances  $\Delta z = \pm 18''$ . Although this percentage decreases, it nevertheless remains in the range of  $70 - 90\%$  at  $-30'' \leq \Delta z \leq 25''$  across most of the radial slices, a result that confirms the detection of spatially resolved molecular gas emission up to vertical distances of about  $1 - 1.5 \text{ kpc}$ . By analyzing the relative variation between the first and second iteration steps in each point of the integrated intensity map, we estimate that the correction converges to within an uncertainty of  $\sim 7\%$ . These

results agree with the error beam contribution to the CO emission in M51 obtained by den Brok et al. (2022). For the rest of this work, we will use the corrected version of the CO map.

Figure 2 illustrates the oscillatory nature of the solution found by the two-step process adopted in this work. The figure compares the three versions of the CO emission detected at a representative high vertical distance above the galaxy midplane  $(\Delta x, \Delta z) = (75'', -30'')$ , corresponding to the uncorrected emission, the emission obtained after the first iteration, and the final version of the spectrum after the second iteration.

## 4. Results

### 4.1. CO moment maps

Figure 3 shows the zeroth, first and second-order moment maps of the CO(2-1) line obtained in the disk and disk-halo interface region of NGC 891, which is mapped in this work. These moment maps were obtained from the data cube version corrected for the error beam contribution, as described in Sect. 3. To derive the zeroth moment map of CO ( $I_{\text{CO}}(\Delta x, \Delta z)$ ), we integrated the emission over the velocity range  $\Delta v_{\text{tot}} = v - v_{\text{sys}} = [-300, 300] \text{ km s}^{-1}$ , encompassing the full extent of velocities due to rotation, as shown in the CO channel maps of Fig. A.1 and A.2. The first and second-order moment maps were derived by applying a  $3\sigma$  clipping to the emission within  $\Delta v_{\text{tot}}$ .

While most of the total CO emission ( $\approx 70\%$ ) stems from a thin, edge-on disk within a range of vertical distances of  $\Delta z \approx \pm 10''$  ( $\pm 475 \text{ pc}$ ), a visual inspection of Fig. 3 shows the detection of statistically significant ( $\geq 3\sigma$ ) CO emission extending to a larger range of vertical distances above and below the galaxy midplane at  $z=0''$ :  $20''$  (1 kpc)  $\leq |\Delta z| \leq 30''$  (1.4 kpc). The lowest-level contours of Fig. 3 reveal a filamentary pattern of the out-of-plane CO emission.

The first moment map shows the mean velocity field of molecular gas. As expected, the kinematics of the gas are dominated by the galaxy's rotation. Gas emission appears blueshifted (redshifted) for  $\Delta x \geq 0''$  ( $\Delta x \leq 0''$ ). The velocity gradient along the galaxy's major axis is steepest within  $|\Delta x| \leq 20''$  due to the presence of high-velocity gas emission from the circumnuclear disk (CND) associated with the  $x_2$  orbits of the stellar bar (García-Burillo & Guélin 1995). A quantitatively similar signature of rotation is imprinted on the gas lying at high vertical distances. In particular, the isovelocity contours are mostly parallel to the galaxy's minor axis outside the CND. This pattern indicates that the out-of-plane molecular gas component shows no rotation lag, unlike the HI emission at large distances (Oosterloo et al. 2007).

The second moment map shows the measured velocity dispersion ( $\sigma_v$ ) of the CO line across the mapped region. The widest lines ( $\sigma_v > 70 \text{ km s}^{-1}$ ) are found close the center of the galaxy, where the steep velocity gradients associated with the CND combined with the high inclination of the disk cause the highest degree of beam smearing. Outside the CND, the velocity dispersion shows a monotonic decline along the major axis. Nevertheless, the gradient of  $\sigma_v$  measured along the minor axis is significant only within the CND region. At larger radii the vertical gradient of  $\sigma_v$  is very shallow. CO lines have comparable widths at different vertical distances for a given  $x$ -offset. Like the CO spectra of the midplane, this suggests that the out-of-plane CO signal also stems from the sum of line emission arising at multiple velocity components along the line of sight.

### 4.2. The thin and the thick molecular gas disks

The distribution and kinematics of molecular gas derived from the CO moment maps presented in Sect. 4.1, provide supporting evidence for the existence of a significant out-of-plane molecular gas component extending to vertical distances of  $\Delta z \approx 1 - 1.5 \text{ kpc}$ . In this section, we model the average out-of-plane distribution of CO emission using Gaussian components to quantify both the vertical extent and mass of the thick molecular disk. Gaussian models are expected to provide a reliable description of the vertical structure of molecular gas under the assumption of hydrostatic equilibrium for the gas disk, which is embedded in the larger-scale external potential of the stellar disk (e.g., Bica et al. 1997).

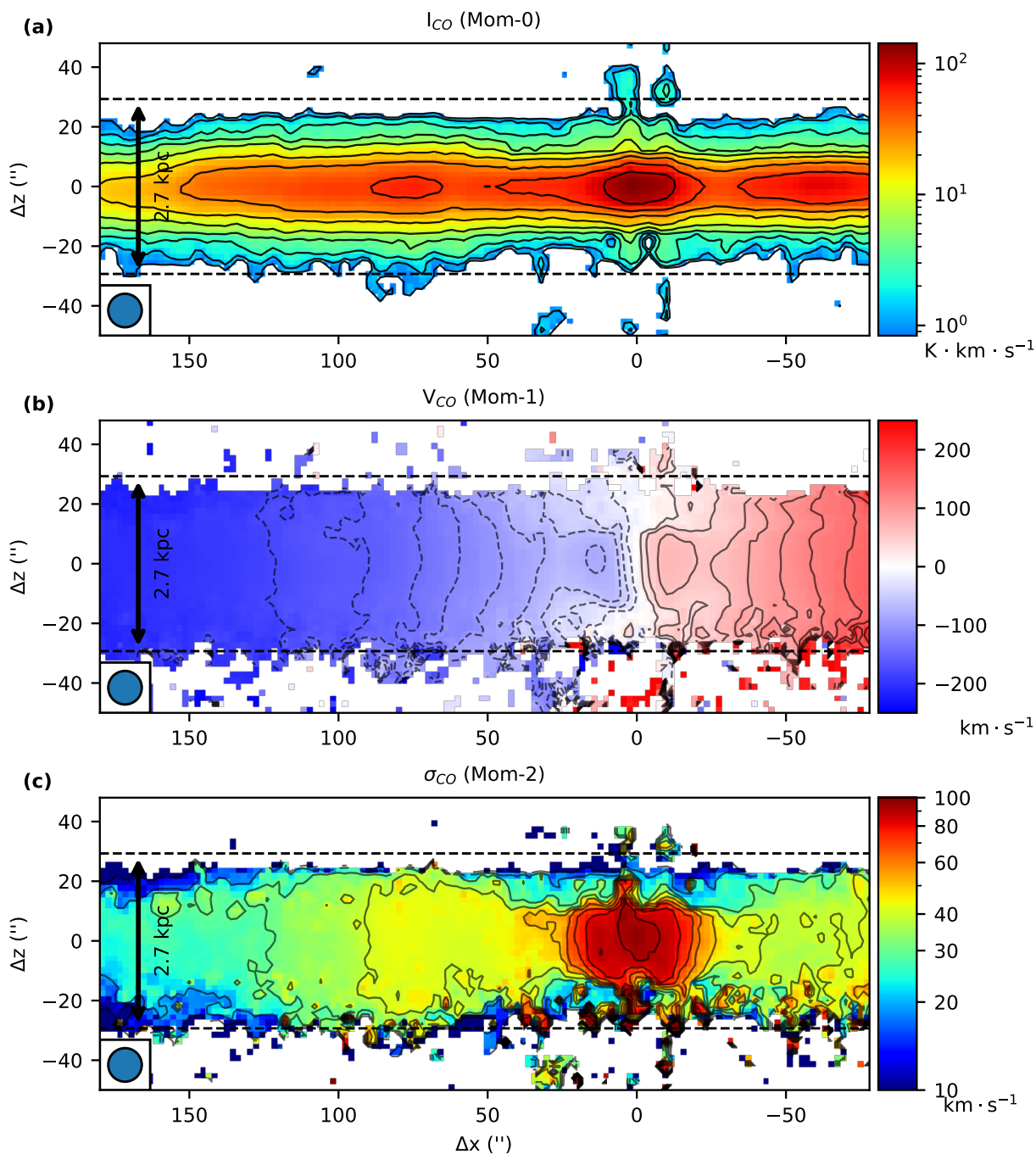
Figure 4 presents the results of fitting the vertical CO distribution shown in Figure 4.1 as a function of the offset along the major axis with a single-Gaussian component. Fig. 4 shows the fitted  $\Delta z$  centroids and the deconvolved  $FWHM$  values of the Gaussians as a function of the offset  $\Delta x$  along the major axis. The Gaussian centroids cluster around a value of  $\Delta z \approx -0.5''$ , which represents a small offset relative to the assumed major axis locus and to our spatial resolution. This offset could be attributed to residual pointing errors of the 30m telescope. The centroids show no significant trend across the full radial extent of the mapped region. However, the evolution of the deconvolved  $FWHM$  values along the major axis shows a significant increase outside the central region:  $FWHM_{[|\Delta x| > 50'']} \approx 13.7''$  (640 pc)  $\approx 1.6 \times FWHM_{[|\Delta x| < 50'']} \approx 8.7''$  (400 pc). The difference in the average thickness of the molecular gas disk can be explained by the deeper gravitational potential in the central region. Although the CO interferometer map of the galaxy published by Scoville et al. (1993) shows no counterpart of the thick molecular disk, the reported thickness ( $FWHM$ ) of the thin disk emission is also found to increase from the galactic nucleus ( $\sim 160 \text{ pc}$ ) to the edge of the galaxy ( $\sim 276 \text{ pc}$ ).

Figure 5 shows the mean out-of-plane CO distribution in the mapped area of NGC 891 ( $\langle I_{\text{CO}} \rangle(\Delta z)$ ), obtained by averaging  $I_{\text{CO}}(\Delta x, \Delta z)$  along the major axis. Figure 5 also presents the results of fitting the observed profile with one and two Gaussian components. The parameters derived from the fits are listed in Table 2.

The  $\langle I_{\text{CO}} \rangle(z)$  profile shows evidence of a thick molecular gas disk that extends to vertical distances of  $|\Delta z| \approx 30''$  (1.4 kpc). The single-Gaussian fit of the  $\langle I_{\text{CO}} \rangle(z)$  profile of  $FWHM = 490 \text{ pc}$  leaves large residuals that are up to  $25\sigma$  ( $\sigma = 58 \text{ mK km s}^{-1}$ ) over a wide range of vertical offsets from  $\pm 12''$  ( $\pm 0.6 \text{ kpc}$ ) to  $\pm 30''$  ( $\pm 1.4 \text{ kpc}$ ). The thickness of the disk determined by the single-Gaussian model is likely overestimated due to the presence of out-of-plane gas, which is inadequately described by the model.

The use of two Gaussian components provides a substantially improved representation of the out-of-plane CO distribution, consisting of a thin disk ( $FWHM = 360 \text{ pc}$ ) and a thick disk ( $FWHM = 1.1 \text{ kpc}$ ). As shown in Fig. 5, the large residuals of the single-Gaussian model disappear at large vertical offsets in the double-Gaussian fit. The full extent of the thick molecular disk measured at a  $3\sigma$  level in  $\langle I_{\text{CO}} \rangle$  is  $\approx 2.7 \text{ kpc}$ . Nonetheless, the double-Gaussian fit overestimates the value of  $\langle I_{\text{CO}} \rangle$  by a factor of  $\approx 2$  in the range of vertical offsets of  $|\Delta z| \approx 1.3 - 1.5 \text{ kpc}$ .

We estimate the fraction of molecular gas mass contained in the thick disk component relative to the total gas mass ( $f_{\text{thick}}$ ) from the Gaussian decomposition described above. A conservative lower limit on  $f_{\text{thick}} \approx 3\%$  is obtained from the normalized



**Fig. 3.** CO moment maps. From top to bottom: the velocity-integrated intensities (*panel a*), the intensity-weighted velocities (*panel b*) and the velocity dispersions (*panel c*) derived from the CO(2–1) line in the mapped region. Contour levels for the CO intensities increase logarithmically from  $3\sigma$  to  $600\sigma$  in steps of 0.26 dex, with  $\sigma = 0.28 \text{ K km s}^{-1}$ . Mean-velocity contours range from  $-180$  to  $180 \text{ km s}^{-1}$  in steps of  $20 \text{ km s}^{-1}$ . Dashed lines indicate negative contour values. Dispersion contours go from  $10$  to  $100 \text{ km s}^{-1}$  in steps of  $10 \text{ km s}^{-1}$ . The  $30 \text{ m}$  beam size ( $11.2''$ ) is indicated as a filled circle in the bottom left corner of each panel. A vertical thickness of  $2.7 \text{ kpc}$  is represented as horizontal dashed lines, as visual reference.

flux of the residuals of the single-Gaussian model, although this likely underestimates the true value. The double-Gaussian model estimates the value of  $f_{\text{thick}}$  to be up to  $\approx 27\%$ . Under the hypothesis that the same CO-to- $\text{H}_2$  conversion factor applies to the thin and the thick disks, we estimate that the thick disk can contribute up to  $\sim 27\%$  of the total molecular gas mass. This fraction is similar to the estimated value of  $\sim 35\%$  for the thick molecular

disk imaged in the CO(1–0) line, as reported in Sofue & Nakai (1993).

#### 4.3. Comparison with other ISM tracers

Sections 4.1 and 4.2 present strong evidence for the presence of a thick molecular disk in NGC 891. In this section we compare the distribution of molecular gas derived from the  $30\text{m}$  CO map with

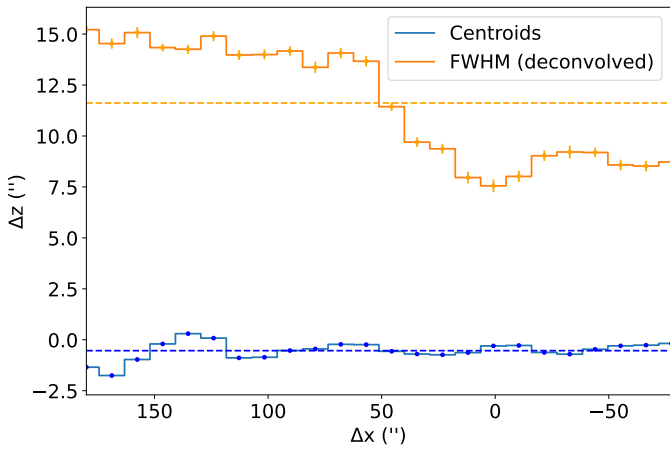


**Fig. 4.** The centroids (blue histogram) and deconvolved  $FWHM$  thickness values (orange histogram) derived from the single-Gaussian fits of the out-of-plane molecular gas distribution across the major axis of the galaxy. The dashed lines show the estimated mean values of  $\Delta z$  and  $FWHM$ . The error bars are derived from the covariance of the parameters from the Gaussian fit.

	CO (2-1)	HI	H $\alpha$
$A_{1G}$	$0.970 \pm 0.008$	$0.823 \pm 0.009$	$0.95 \pm 0.01$
$FWHM_{1G}$ [kpc]	$0.49 \pm 0.01$	$1.49 \pm 0.02$	$1.25 \pm 0.02$
$\Delta z_{3\sigma}$ [kpc]	2.07	4.45	3.12
$A_{2G}$	$1.008 \pm 0.006$	$0.956 \pm 0.004$	$0.995 \pm 0.006$
$A_{thin}$	$0.73 \pm 0.04$	$0.586 \pm 0.006$	$0.19 \pm 0.01$
$A_{thick}$	$0.27 \pm 0.04$	$0.414 \pm 0.006$	$0.81 \pm 0.01$
$FWHM_{thin}$ [kpc]	$0.36 \pm 0.02$	$1.15 \pm 0.01$	$0.53 \pm 0.02$
$FWHM_{thick}$ [kpc]	$1.1 \pm 0.1$	$3.91 \pm 0.07$	$1.60 \pm 0.02$
$\Delta z_{thick,3\sigma}$ [kpc]	3	10	3.8

**Table 2.** Results obtained from the single-Gaussian (1G) and double-Gaussian (2G) fits of the average out-of-plane profiles of CO, HI and H $\alpha$ .  $A_{1G,2G}$  represent the fraction of the observed flux in the profiles that is accounted for by the fitted components,  $FWHM_{1G,2G}$  are the deconvolved full widths at half maximum of each component,  $\Delta z_{3\sigma}$  are the full widths of the fitted components measured at a  $3\sigma$  level. The table also includes the values for the parameters of the thin and thick Gaussian fitting curves of the two-components model.

that derived from other tracers of the ISM, namely the neutral atomic hydrogen (HI), the diffuse ionized gas (DIG; H $\alpha$ ), and the dust, in order to identify possible counterparts of the thick molecular disk of NGC 891.

Figure 6 shows the velocity-integrated CO intensity contours overlaid on the HI zeroth-moment map from Oosterloo et al. (2007), as well as on the H $\alpha$  and unsharp-masked (USM) V-band images from (Howk & Savage 2000) of the galaxy, over the region mapped in this work.

The HI emission, derived from the high-resolution dataset of the HALOGAS survey (Heald et al. 2011), extends to large vertical distances far beyond the molecular component. At vertical distances of  $\Delta z \gtrsim 6$  kpc, namely a factor of 4 larger than the maximum extent of CO in the thick disk, HI remains detectable. The low-resolution HI data of the galaxy of Oosterloo et al. (2007) reveal filamentary structures of the gas that reach heights of up to  $\sim 22$  kpc. For the purposes of comparison with the CO data, we focus on the high-resolution HI map, whose beam size ( $FWHM_{HI,HR} = 23.4'' \times 16''$ ) is more comparable to that of the CO observations ( $FWHM_{CO} = 11.2'' \times 11.2''$ ). At  $\Delta z \sim 1.5$  kpc, where CO emission drops below the detection threshold of the observations, the HI emission remains fairly uniform across galactocentric radius.

The DIG distribution, traced by H $\alpha$  emission from Kamphuis et al. (2007), shows a total vertical extent comparable to that of the molecular gas. The same conclusion can be drawn by comparing the CO map with the H $\alpha$  image published by Howk & Savage (2000). The H $\alpha$  emission exhibits an asymmetric distribution within the plane of the galaxy along its major axis, with comparatively stronger emission observed on the northeastern (approaching) side of the disk. This asymmetry is attributable to the location of the HII regions, which are positioned inside corotation, downstream from the spiral arm on the approaching side of the galaxy's disk (García-Burillo et al. 1992). Conversely, HII regions on the southwestern side of the disk would suffer from the high extinction associated with the spiral arm. Significant extraplanar emission is detected above and below regions of enhanced star formation. Both CO and H $\alpha$  reach similarly large vertical distances near the galactic center and on the northeastern side of the disk, suggesting a close connection between local star formation activity in the disk and the vertical extent of the gas.

To quantify the vertical structure of the different ISM tracers in NGC 891, we compared the performance of single-Gaussian (thin disk only) and double-Gaussian (thin+thick disk) models in reproducing the averaged vertical profiles of HI, and H $\alpha$  emission, adopting a methodology similar to that used to analyze the CO data in Sect. 4.2. The resulting best-fit parameters are summarized in Table 2, and the corresponding fits are shown in Fig. 7. The molecular and ionized gas exhibit remarkably similar vertical extents, while the HI distribution extends significantly to larger vertical distances farther into the halo.

The improvement achieved by adopting a double-Gaussian model to reproduce the vertical structure of HI and H $\alpha$  emission is most clearly seen in the residuals (see Fig. B.1). The CO and DIG maps exhibit a similar vertical structure, with detectable emission extending to  $\Delta z_{3\sigma}^{HI} \approx 3.8$  kpc. The HI gas shows the most extended distribution, characterized by a thin disk with  $FWHM \sim 1.1$  kpc and a thick disk with  $FWHM \sim 3.9$  kpc, reaching  $\Delta z_{3\sigma}^{HI} \approx 10$  kpc. Yim et al. (2011) also concluded that the inclusion of a second thick Gaussian component improves the fit of the observed vertical structure of the HI gas. These results highlight the progressively increasing vertical extent of the ISM phases from molecular and DIG to atomic gas.

#### 4.4. Kinematics: Position-Velocity Diagrams

To investigate the kinematics of the molecular gas, we constructed a position-velocity (PV) diagram of the CO(2-1) emission along the major axis of NGC 891 at  $\Delta z = 0$  (Fig. 8). The PV diagram clearly reveals the molecular ring and the fast-rotating inner nuclear disk. The latter is confined to the region  $-15'' < \Delta x < +15''$  and reaches velocities of up to  $|v - v_{sys}| \approx 295$  km s $^{-1}$ . A gap separates this central component from the large-scale disk rotation. García-Burillo et al. (1992) and García-Burillo & Guelin (1995) interpreted the X-shaped morphology of the CO position-velocity (PV) diagram as evidence that a stellar bar drives the gas flow. In the model of García-Burillo & Guelin (1995), the bar has a corotation radius of  $r \approx 70''$  (3.3 kpc) and is viewed at an angle  $\alpha \approx 45^\circ$  from the galaxy's major axis. In this scenario, the molecular gas populates the  $x_2$  orbits within a fast-rotating nuclear disk. This disk lies between the two Inner Lindblad Resonances (ILR) of the bar. Outside the nuclear disk, most of the CO emission in the PV diagram is associated with  $x_1$  orbits within the bar up to  $\Delta x = \pm 70'' \times \cos(\alpha) \approx \pm 50''$ , as well as with the spiral arms that develop outside the bar at larger radii.

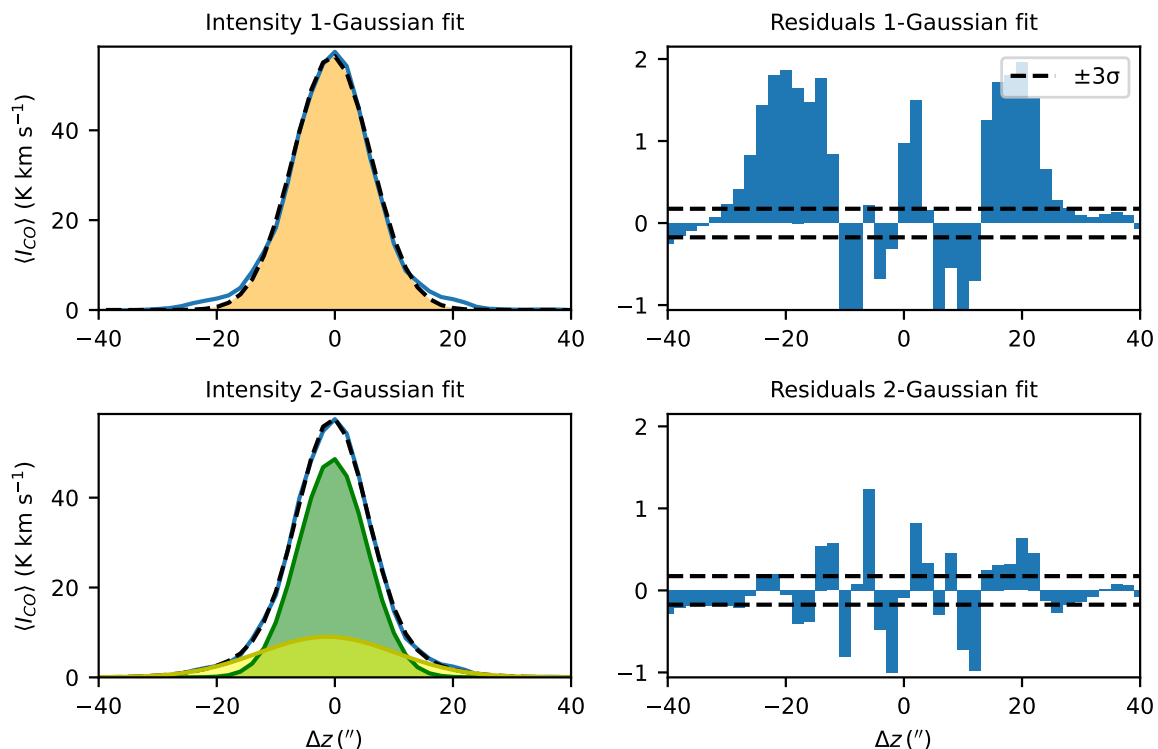


**Fig. 5.** Comparison of the average out-of-plane distribution of CO ( $\langle I_{\text{CO}} \rangle(\Delta z)$ ) with the fits of the single-Gaussian (*upper panels*) and double-Gaussian (*lower panels*) decomposition models described in Sect. 4.2. The blue curve shows the observed profile  $\langle I_{\text{CO}} \rangle(\Delta z)$ . The green and yellow curves in the *lower left panel* show the fit of the thin and thick molecular disk components of the double-Gaussian fit, respectively. The black dashed curves represent the sum of all the components in both models. The *upper* and *lower right panels* display the residuals of the fits. Horizontal dashed lines indicate the  $\pm 3\sigma$  levels with  $\sigma = 58 \text{ mK km s}^{-1}$ .

Figure 9 compares the CO PV diagram with those derived from HI and  $H\alpha$  emission. We extracted PV slices parallel to the midplane at different  $\Delta z$  offsets. The  $H\alpha$  PV diagram is dominated by a solid-body rotation pattern, consistent with previous results by Kamphuis et al. (2007). Notably, there is no  $H\alpha$  emission at high velocities in the nuclear disk. In addition, the  $H\alpha$  PV diagram shows a marked east-west asymmetry. Both characteristics can be attributed to the strong extinction in the galaxy’s midplane. In contrast, the CO emission shows prominent high-velocity features in the nuclear disk, which progressively disappear at larger vertical distances. Outside the inner region, the overall shape of the CO PV diagram transitions towards a structure similar to that of the DIG at higher  $\Delta z$ . The HI emission extends to larger radial distances, particularly on the southwestern side, but exhibits a less pronounced high-velocity component in the nuclear disk. This fast-rotating component rapidly vanishes in slices above and, more noticeably, below the midplane, indicating that it is confined to the thin inner disk, as noted by Oosterloo et al. (2007).

To explore the vertical dependence of the kinematics, we also extracted vertical PV slices at fixed radial offsets and examined spectra at different heights above the midplane. Figure 10 shows representative slices at  $\Delta x = \pm 75''$  for CO and HI, regions well beyond the galactic center. While the H I spectra show a systematic shift of the velocity peaks toward lower absolute velocities with increasing  $|\Delta z|$ , indicative of a rotational lag ( $\sim 15 \text{ km s}^{-1} \text{ kpc}^{-1}$ ; Oosterloo et al. 2007), no such trend is observed in the molecular gas within the range of vertical distances where CO emission is detected. At  $\Delta x = \pm 75''$ , additional intensity peaks appear at lower velocities than the terminal velocity at

these radii. These features likely correspond to prominent spiral arm segments that develop outside the bar. The kinematic signature of the spiral arm becomes visible near  $\Delta x \simeq \pm 70''$ , subsequently merging with the terminal velocity of the main disk at larger radii. Notably, the vertical extent of CO emission shows little dependence on velocity. This suggests that the vertical extent of molecular gas is comparable inside and outside the spiral arms.

Figs.C.1, C.2, & C.3 show additional CO, HI, and  $H\alpha$  PV slices in Appendix C

## 5. Discussion

### 5.1. The thick disk: effect of inclination on the observed vertical extent

Although the literature reports values for the inclination of the disk of NGC 891 ( $i \simeq 88 - 89^\circ$  Rupen 1991; Garcia-Burillo et al. 1992; Sofue & Nakai 1993) indicating an edge-on orientation of the galaxy, it is important to assess whether the projection effects of a tilted disk could artificially produce or enhance the appearance of a vertically extended component of molecular gas. In particular, the emission from gas at different galactocentric radii along the line of sight could mimic an increased vertical thickness.

In order to evaluate this effect, we constructed a set of disk models with different inclinations using the  $^3\text{D}$ BAROLO package (Di Teodoro & Fraternali 2015). To this end, we assumed a simple geometrical model of a purely thin molecular disk with a thickness comparable to that of the Milky Way ( $FWHM \sim 250 \text{ pc}$ ). As rotation curve we adopted the one used

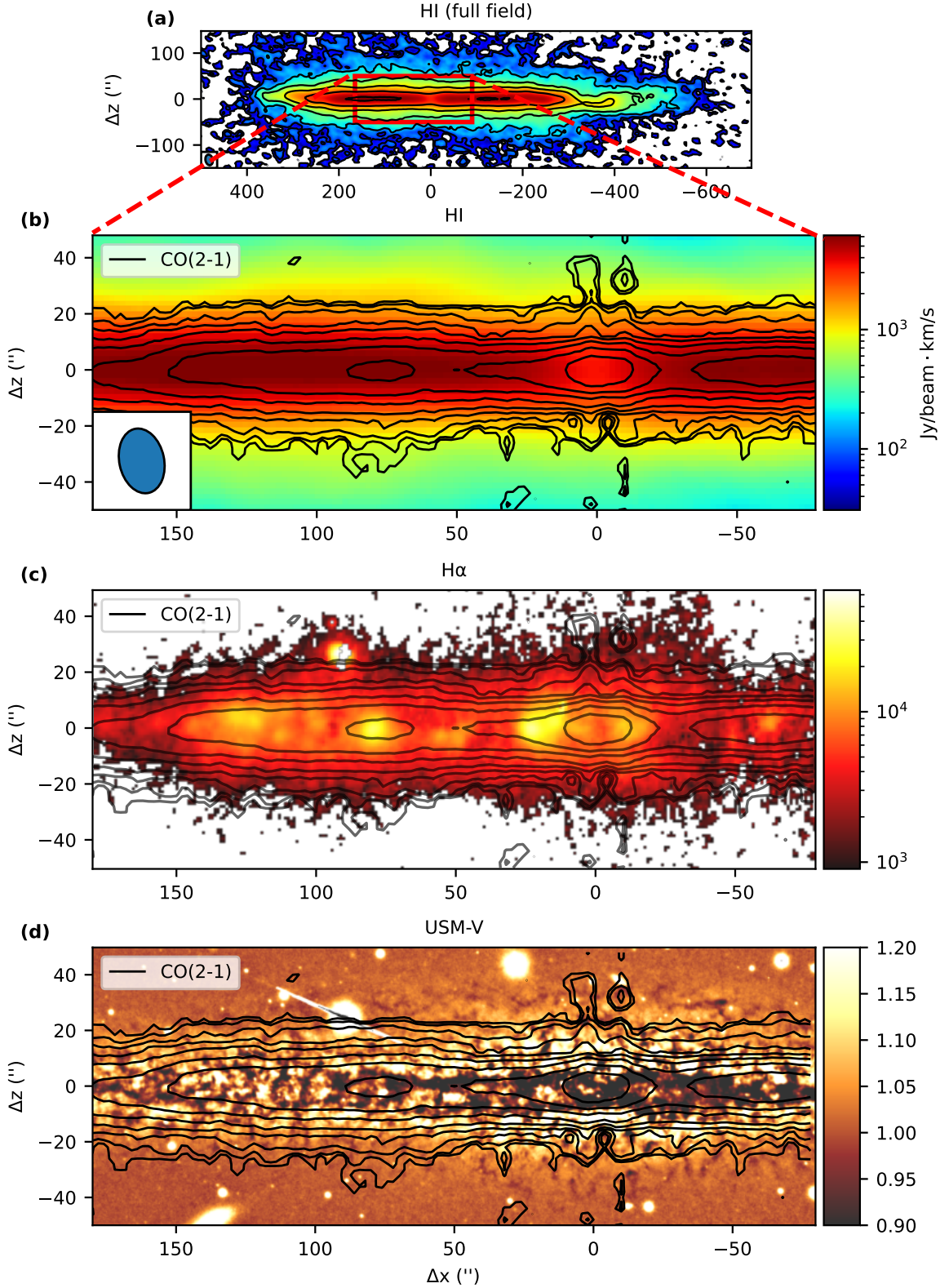


**Fig. 6.** Comparison of the CO map with images obtained in other tracers of the ISM in NGC 891. *Panel a* shows the HI map obtained by Oosterloo et al. (2007) from their full-resolution dataset (in logarithmic color scale and contours from  $3\sigma$  to  $600\sigma$  in steps of 0.38 dex, with  $\sigma = 10.25 \text{ Jy beam}^{-1} \text{ km s}^{-1}$ ). The blue-filled ellipse in the lower left corner of the panel represents the beam of the HI observations ( $23.4'' \times 16'' @ PA = 12.3^\circ$ ). The remaining panels, from top to bottom, show the overlay of the CO intensities (in contours) with (in color scale) the HI image (*panel b*), the H $\alpha$  image from Kamphuis et al. (2007) (*panel c*, arbitrary units), and the USM V-band image from Howk & Savage (2000) (*panel d*) in the region of NGC 891 mapped in this work. The CO contours in all the panels are the same as in Figure 3, covering the same field of view.

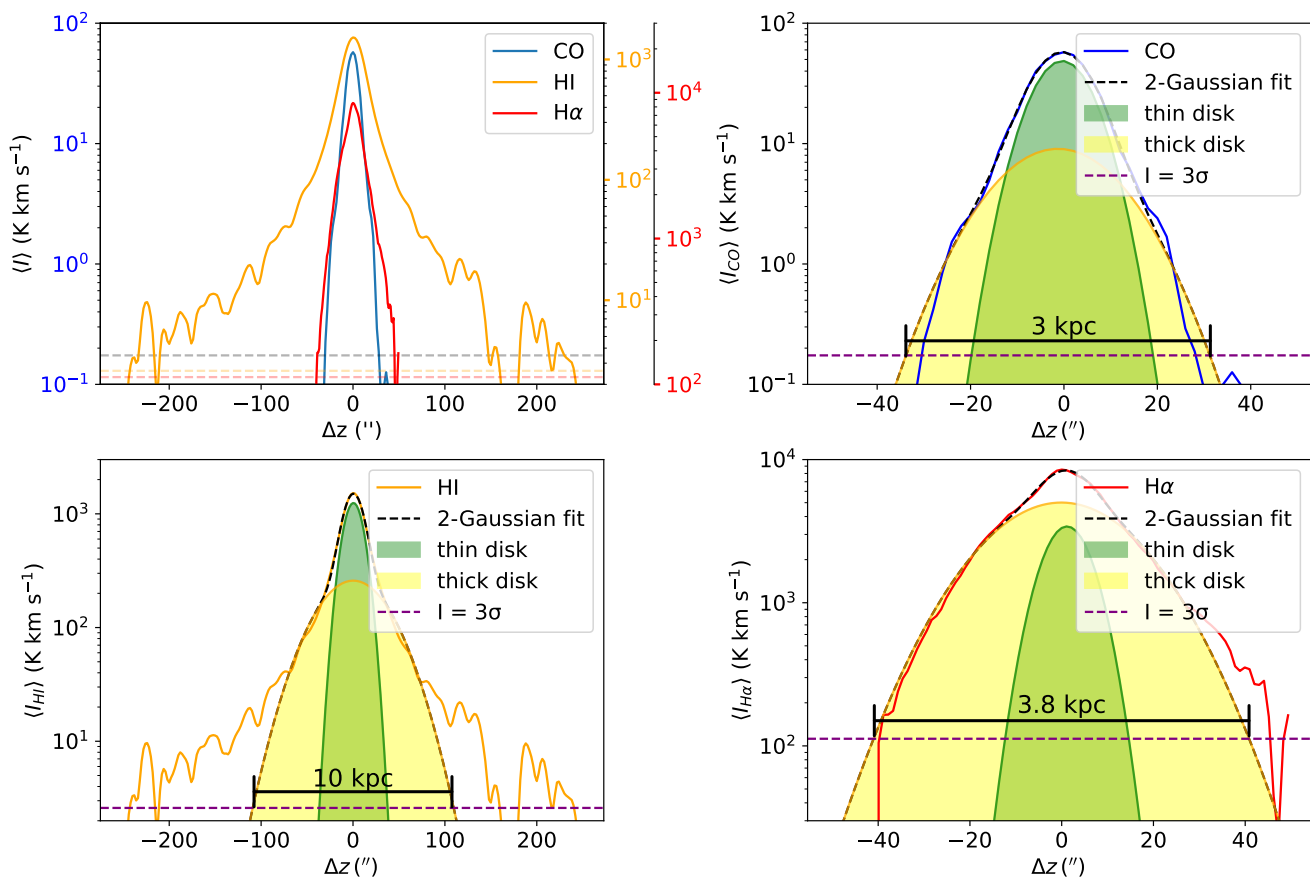


**Fig. 7.** *Upper left panel:* Comparison of the average out-of-plane profiles of CO, HI, and H $\alpha$ . All panels display the y-axis in logarithmic units. The integration ranges over the x-axis used to derive the profiles [ $\Delta x_{\min}$ ,  $\Delta x_{\max}$ ] are: [180'', -80''] for CO, [1150'', -1050''] for HI, and [180'', -80''] for H $\alpha$ . *Upper right panel:* Results of the double-Gaussian fit (black dashed line) of the CO profile (blue solid line). The thin disk and thick disk Gaussian components are shown in green and yellow lines, respectively. *Lower panels:* Same as *Upper right panel* but for the HI and H $\alpha$  profiles. Horizontal dashed lines show the  $3\sigma$  thresholds for each tracer in all panels ( $\sigma_{\text{CO}} = 58 \text{ mK km s}^{-1}$ ,  $\sigma_{\text{HI}} = 864 \text{ mK km s}^{-1}$ , and  $\sigma_{\text{H}\alpha} = 37 \text{ K km s}^{-1}$ ).

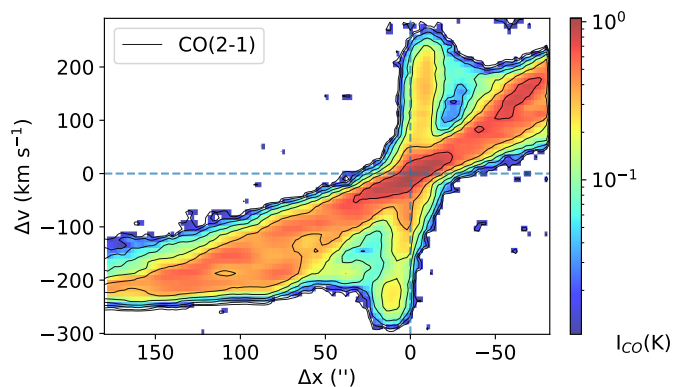


**Fig. 8.** Position-velocity (PV) diagram of the CO(2-1) emission along the major axis at  $\Delta z=0$ . Black line contours are  $3\sigma_{\text{ch,CO}}$ ,  $6\sigma_{\text{ch,CO}}$ ,  $12\sigma_{\text{ch,CO}}$ ,  $24\sigma_{\text{ch,CO}}$ ,  $48\sigma_{\text{ch,CO}}$ ,  $96\sigma_{\text{ch,CO}}$  and  $192\sigma_{\text{ch,CO}}$  ( $\sigma_{\text{ch,CO}} = 3.5 \text{ mK}$ ). The blue dashed lines indicate the location of the dynamical center in the parameter space of the PV diagram.

by Garcia-Burillo et al. (1992) to fit the kinematics of molecular gas along the galaxy's major axis:

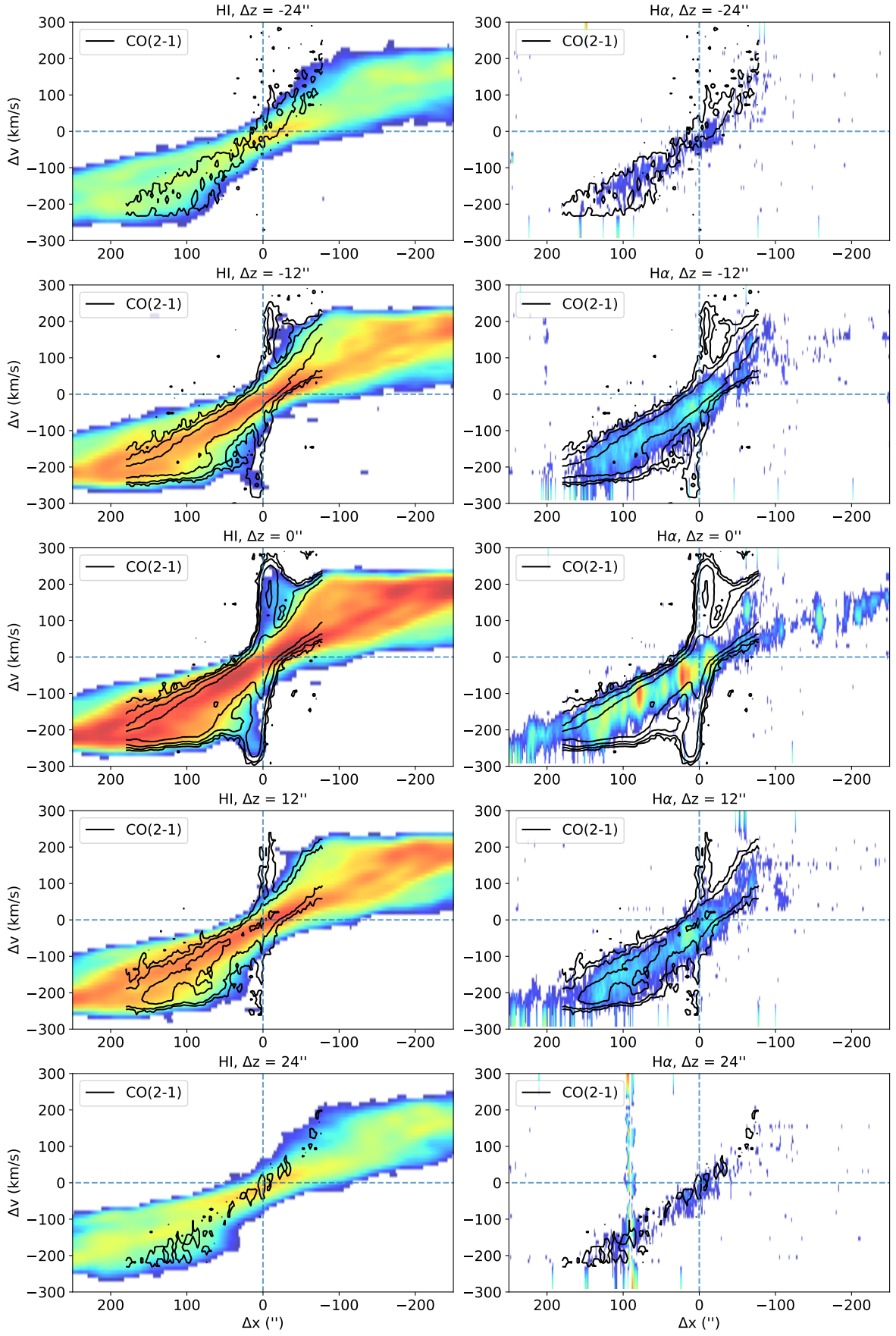
$$v_{\text{rot}} = v_{\text{max}} \cdot \sqrt{\frac{x^2}{x^2 + d^2}} \quad (8)$$

where  $d = 200 \text{ pc}$  and  $v_{\text{max}} = 225 \text{ km}\cdot\text{s}^{-1}$  is the maximum rotational velocity.

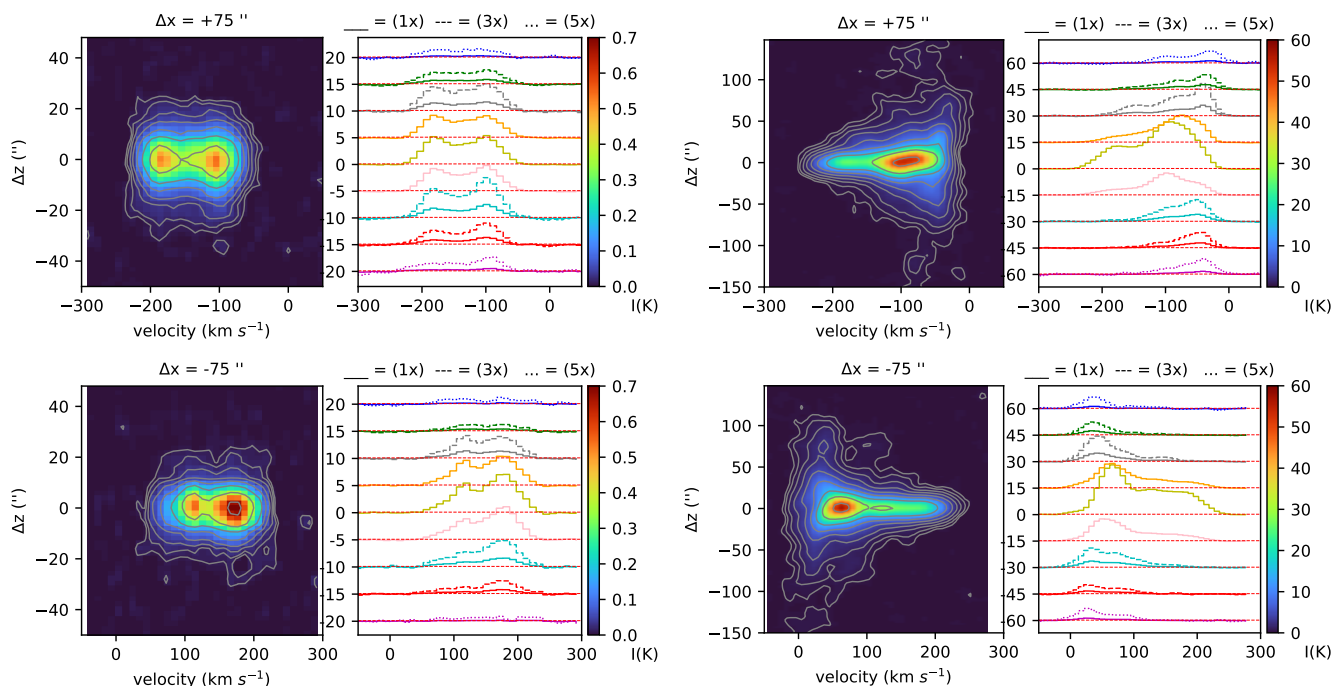
Given the radial extent of the CO disk,  $\approx 250''$  (Garcia-Burillo et al. 1992), an inclination of  $i \approx 83^\circ$  would be necessary to account for the observed vertical extent ( $\approx 30''$ ) of the thin disk (of  $\approx 5'' \approx 250 \text{ pc}$ -size) seen in projection.

Figure 11 shows the resulting simulated vertical PV plots taken at a subset of  $\Delta x$  offsets along the major axis for values of the inclination  $i = 83^\circ$ ,  $85^\circ$ , and  $88^\circ$ . The PV plots derived for  $i = 83^\circ$ , the largest inclination that could explain the observed pattern of the CO emission. The PV plots for  $i = 83^\circ$  show that the emission of the gas at the outer edges of a rotating thin disk, seen in projection at  $\Delta z \sim 15'' - 30''$ , should be closer to the systemic velocity than the gas at the major axis, seen at  $\Delta z \sim 0''$ . This velocity gradient is not consistent with the observations. Even under extreme assumptions, projection effects alone cannot account for the detected emission at  $|\Delta z| \gtrsim 1 \text{ kpc}$ . This result confirms that the identified thick molecular disk is not an artifact of inclination, but represents a genuine extraplanar component.

Swaters et al. (1997) reached a similar conclusion regarding the inclination of the HI gas disk. While an inclination of  $\approx 80^\circ$  would be required to explain the observed HI thickness of the galaxy, a tilted disk at  $< 86^\circ$  produced a V-shaped signature in the PV plots that was more pronounced than in the observations.



**Fig. 9.** PV slices parallel to the galactic plane of the HI (left) and H $\alpha$  (right) emissions. Slices are taken at  $\Delta z = 0''$ ,  $12''$  and  $24''$  above and below the midplane. Color scales are clipped at  $3\sigma_{\text{ch}}$  ( $\sigma_{\text{ch,HI}} = 147$  mK,  $\sigma_{\text{ch,H}\alpha} = 3.8$  K). PV slices of the CO(2-1) emission are plotted as black contours, with levels  $3\sigma_{\text{ch,CO}}$ ,  $9\sigma_{\text{ch,CO}}$ ,  $27\sigma_{\text{ch,CO}}$  and  $81\sigma_{\text{ch,CO}}$  ( $\sigma_{\text{ch,CO}} = 3.5$  mK). Dashed blue lines denote the zero-offset coordinates.



**Fig. 10.** Position-velocity vertical slices of CO (left panels) and HI (right panels) at  $\Delta x = \pm 75''$ . Contours increase logarithmically from  $3\sigma_{\text{ch}}$  to  $600\sigma_{\text{ch}}$  ( $\sigma_{\text{ch,CO}} = 3.5$  mK,  $\sigma_{\text{ch,HI}} = 148$  mK) in steps of 0.26 dex. Next to the PV slices we show the CO and HI spectra observed at different vertical  $\Delta z$  offsets. Some of the spectra have been rescaled for clarity. The red dotted horizontal line denotes the  $3\sigma_{\text{ch}}$  detection limit.

## 5.2. The thick molecular disk and the galactic fountain scenario

An order-of-magnitude estimate of the timescales involved in lifting molecular gas into the halo can provide further insight into the physical mechanisms that explain the observed properties of the thick disk.

The time required for molecular gas to reach the characteristic maximum height of  $z_{\text{max}} \sim 1.5$  kpc derived from the observations,  $t_{\text{lift}}$ , can be estimated if we assume a value for the kick vertical velocity ( $v_{\text{kick}}$ ). Fraternali & Binney (2006) modeled the extra-planar HI gas of NGC 891 assuming that gas clouds act as non-interacting particles lifted from the plane of the disk due to the expansion of superbubbles inflated by supernovae. The velocity required to reproduce the distribution of the HI halo in Fraternali & Binney (2006) model is  $\approx 75$  km s $^{-1}$ . This value is in close agreement with the predictions of hydrodynamical models of Mac Low & McCray (1988). Therefore, if we assume  $v_{\text{kick}} = 75$  km s $^{-1}$ :

$$t_{\text{lift}} \approx \frac{z_{\text{max}}}{v_{\text{kick}}} \approx 20 \text{ Myr}. \quad (9)$$

This timescale is comparable to the lifetimes of massive stars and to the duration of active star-forming episodes ( $t_{\text{SF}} \approx 10$  Myr), which supports the idea that stellar feedback can plausibly sustain the observed thick molecular disk. If the molecular gas subsequently cools and falls back toward the disk, the full fountain cycle would occur on timescales of a few tens of Myr.

Star formation activity in the disk is expected to be assembled along the spiral arms of the galaxy. In the event that the two-spiral arm structure of NGC 891 is coupled to the galaxy's stellar bar, it can be posited that both density wave features would exhibit an identical pattern speed, given by  $\Omega_{\text{p}} = \frac{v_{\text{rot}}}{R_{\text{cor}}}$ , where  $R_{\text{cor}} \approx 70''$  (3.3 kpc) is the bar's corotation radius, determined by Garcia-Burillo & Guélin (1995). The rotation of the two-spiral

arm pattern would propagate star formation in the disk with an associated timescale ( $t_{\text{rot}}$ ) given by the following relation

$$t_{\text{rot}} = \frac{1}{2} \frac{2\pi}{\Omega_{\text{p}}} \approx 45 \text{ Myr} \quad (10)$$

This is the timescale over which the two-spiral-arm pattern of NGC 891 would sweep through the disk, producing mixing and triggering star formation as gas passes through the  $m = 2$  density wave. The mixing induced by the spiral pattern on timescales of a few tens of Myr can account for the comparable vertical extent of molecular gas inside and outside the spiral arms, as discussed in Sect. 4.4. The observed extraplanar CO emission along a given line of sight would therefore trace the cumulative effect of multiple ejection events over the past few tens of Myr. This picture is further supported by recent studies showing that star formation in disk galaxies is not confined to spiral arms, with a significant fraction occurring in interarm regions and contributing to the spatial diffusion and mixing of stellar feedback across the disk, in addition to the redistribution driven by disk rotation (e.g., Foyle et al. 2010; Kreckel et al. 2016; Querejeta et al. 2021, 2024).

Although these estimates are necessarily approximate and rely on simplified assumptions regarding the vertical velocity and gravitational potential, their similarity within a factor of a few demonstrates that the presence of a thick molecular component extending up to  $\sim 1.5$  kpc is fully consistent with a galactic fountain scenario operating under typical disk conditions in NGC 891.

A detailed inspection of the CO channel maps shown in Figs. A.1 & A.2 shows that the largest vertical extents of molecular gas occur predominantly in the northeastern half of the galaxy. In several channels (e.g.,  $v_{\text{ch}} = -125$  and  $-175$  km s $^{-1}$ ), CO emission reaches heights of  $\sim 40$ – $45''$  (1.8–2.0 kpc) below the midplane. These regions coincide spatially with prominent dust filaments identified in the unsharp-masked optical images

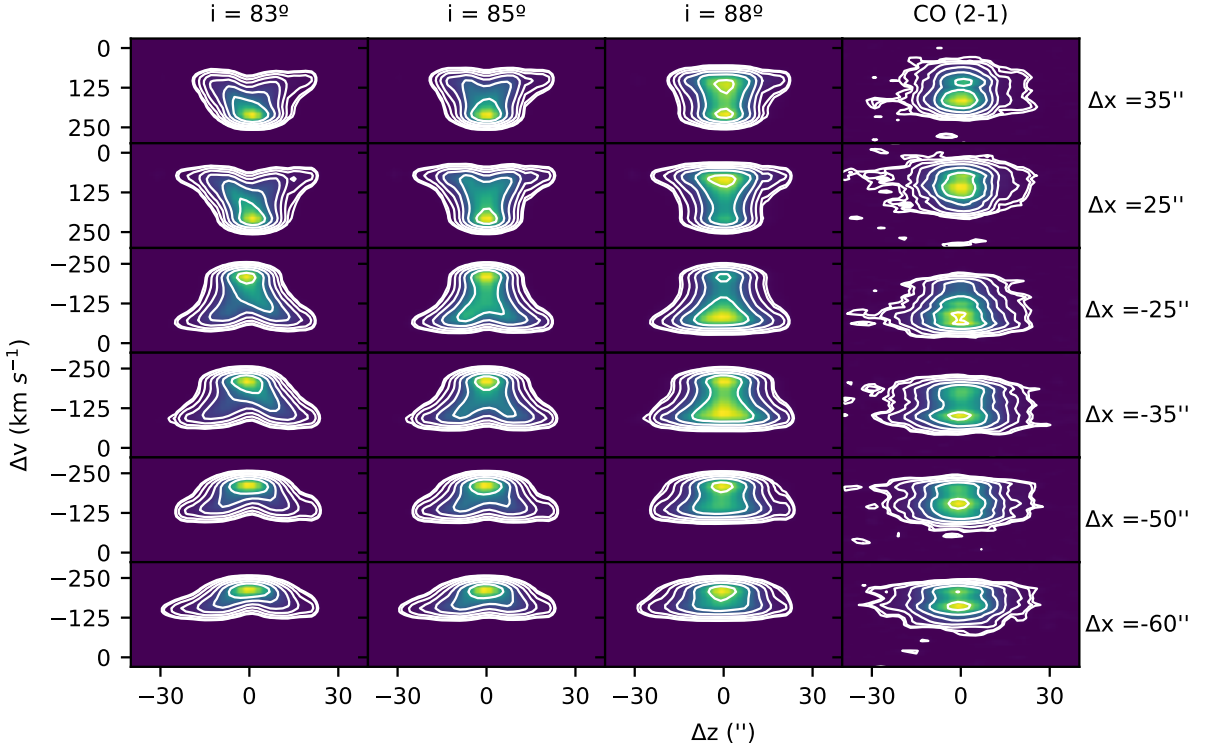


**Fig. 11.** Position-velocity (PV) vertical slices at different radial offsets  $\Delta x$  and for different galaxy inclinations obtained by  $3^D$ BAROLO. For each PV slice the horizontal axis is the  $\Delta z$  offset in " and the vertical axis is the velocity towards the observer in  $\text{km s}^{-1}$  relative to  $v_{\text{sys}}$ . The right-most column represents the PV slice that was obtained from the observations. White contours show the levels  $3\sigma_{\text{ch,CO}}$ ,  $4\sigma_{\text{ch,CO}}$ ,  $8\sigma_{\text{ch,CO}}$ ,  $16\sigma_{\text{ch,CO}}$ ,  $32\sigma_{\text{ch,CO}}$ ,  $64\sigma_{\text{ch,CO}}$ , and  $128\sigma_{\text{ch,CO}}$ .

of Howk & Savage (2000) and with enhanced diffuse ionized gas emission traced by  $\text{H}\alpha$ . Chasten et al. (2024) used NIR-Cam imaging at 1.5 and 2.7  $\mu\text{m}$  to reveal a tight connection between dust filaments and star-forming regions in the midplane of NGC 891, extending into the lower halo. Together with the CO and  $\text{H}\alpha$  data presented here, these results indicate that the thick molecular disk is primarily shaped by feedback-driven outflows associated with disk star formation.

The close spatial and kinematic correspondence between molecular gas, ionized gas, and dust strongly suggests that these components are linked by a common physical mechanism. In particular, the observed morphology is consistent with a galactic fountain scenario, in which stellar feedback from star-forming regions drives gas vertically from the disk into the halo. In this framework, molecular gas is entrained together with dust and ionized material, reaching moderate heights before cooling and returning to the disk. The dust distribution, highlighted using the USM V-band image, reveals numerous dark filaments ('chimneys') emerging from the midplane and extending to large vertical distances into the halo. A detailed comparison between the chimneys and the molecular gas features of the thick CO disk is not possible due to the significantly different spatial resolutions of these observations. However, the network of dark filaments is distributed over spatial scales comparable to those of the thick CO disk. Several of these filaments are spatially coincident with regions of enhanced CO and  $\text{H}\alpha$  emission. In particular, prominent structures near  $\Delta x \approx 100''$  and  $140''$  extend to heights of  $\sim 2$  kpc, comparable to the vertical extent of the molecular and ionized gas. Similar features were previously reported by Howk & Savage (2000) and more recently by Chasten et al. (2024). A galactic fountain mechanism

(Fraternali & Binney 2006) is likely responsible for most of the gas at heights of  $z \leq 5$  kpc, whereas the outermost regions may contain  $\sim 10\%$  of the halo gas, probably originating from accretion processes (Oosterloo et al. 2007).

Alternative explanations involving external accretion appear less likely for the molecular component. While Oosterloo et al. (2007) reported signatures of gas accretion in NGC 891 in the form of counter-rotating HI clouds and a large filament extending up to  $\sim 22$  kpc from the disk, these structures occur at much larger heights than those probed by the molecular gas. The limited vertical extent of the thick molecular disk detected here suggests that inflow processes are not dynamically dominant at these heights.

## 6. Summary and conclusions

We present new CO(2–1) observations of the nearby edge-on spiral galaxy NGC 891 carried out with the IRAM 30m telescope. These observations provide unprecedented sensitivity and spatial coverage of the molecular gas distribution in the disk and the disk-halo interface of the galaxy. This project builds on the previous work of García-Burillo et al. (1992) who found evidence for CO emission extending over 1 kpc outside the galactic plane of NGC 891.

Our main conclusions can be summarized as follows:

1. We confirm the detection of a vertically extended molecular gas component or thick disk by robustly characterizing and correcting for the residual error-beam contamination in the observations using an iterative approach.
2. The vertical distribution of molecular gas is best fit by a double-Gaussian component, consisting of a bright thin disk,

- with deconvolved  $FWHM \simeq 360$  pc, and a fainter thick disk, with deconvolved  $FWHM \simeq 1.1$  kpc. Statistically significant emission is detected in a region extending up to vertical distances of  $\lesssim 1.3 - 1.4$  kpc at the  $3\sigma$  level.
3. Under the hypothesis that the same CO-to-H<sub>2</sub> conversion factor applies to the thin and the thick disks, we estimate that the thick disk can contribute up to  $\sim 27\%$  of the total molecular gas mass.
  4. The vertical extent of the molecular gas is comparable to that of the diffuse ionized gas, but significantly smaller than that of the neutral atomic hydrogen, which dominates the budget of neutral gas in the halo at larger heights.
  5. The molecular thick disk shows no evidence for a significant vertical rotation lag, in contrast to the HI component. The distribution and kinematic properties of the extraplanar CO gas indicate that this component traces the cumulative effect of multiple gas ejection events driven by star formation in the disk over the past few tens of Myr.
  6. The spatial association between molecular gas, ionized gas, and dust filaments, together with the limited vertical extent and kinematic properties, strongly favors a stellar-feedback-driven galactic fountain as the dominant mechanism shaping the thick molecular disk. Alternative scenarios involving external accretion, which are required to explain the properties of the HI gas extending up to  $\sim 22$  kpc from the disk, appear less likely for the molecular component.

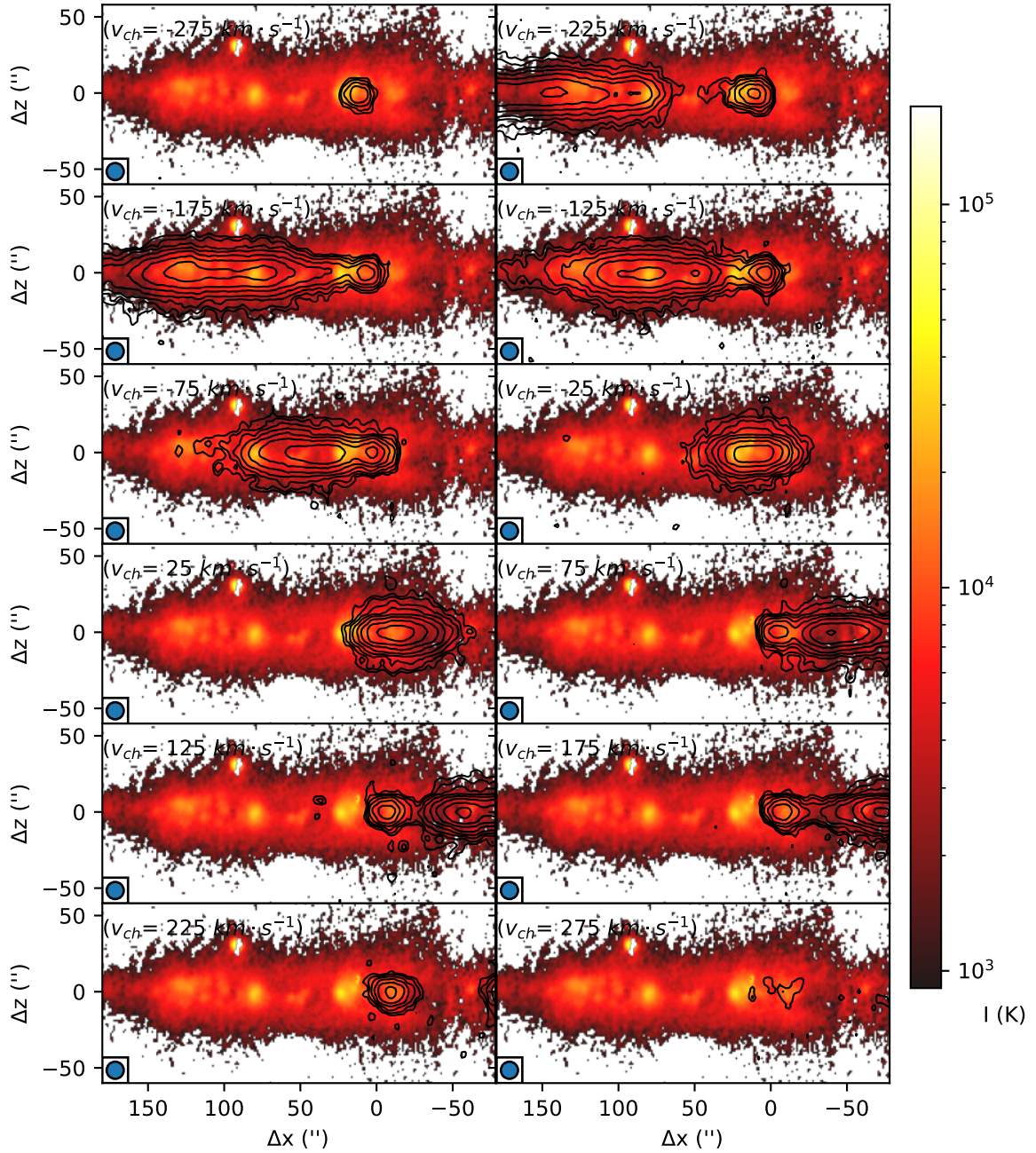
These results demonstrate that molecular gas can be efficiently lifted into the halo of non-active and non-starburst disk galaxies, where it participates in disk-halo cycling processes. Interferometric observations that do not include a zero-spacing correction would filter out the existence of low-level CO emission coming from putative thick disk components. Future high-sensitivity observations combining single-dish and interferometric data from an additional sample of edge-on galaxies will be crucial in assessing how common thick molecular disks are, and in quantifying their role in galaxy evolution.

*Acknowledgements.* DJL, SGB, MQ, AU and PT acknowledge support from the Spanish grant PID2022-138560NB-I00 funded by MICIU/AEI/10.13039/501100011033/FEDER, EU. This work is based on observations carried out with the IRAM 30m telescope. IRAM is supported by INSU/CNRS (France), MPG (Germany) and IGN (Spain).

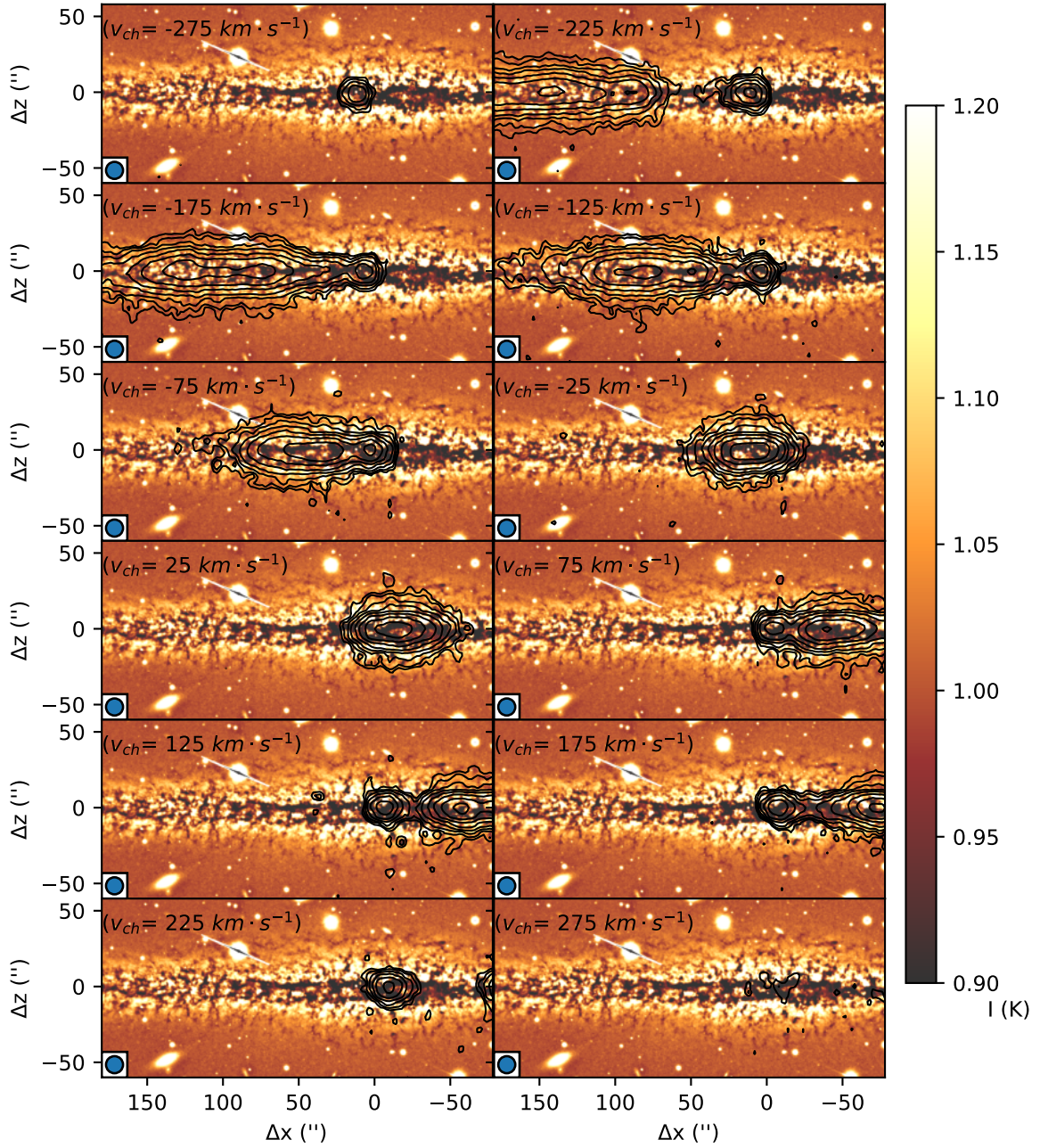
## References

Aalto, S., Garcia-Burillo, S., Muller, S., et al. 2015, *A&A*, 574, A85  
Aalto, S., Garcia-Burillo, S., Muller, S., et al. 2012, *A&A*, 537, A44  
Armillotta, L., Fraternali, F., & Marinacci, F. 2016, *MNRAS*, 462, 4157  
Barcos-Muñoz, L., Aalto, S., Thompson, T. A., et al. 2018, *ApJ*, 853, L28  
Becquaert, J. F. & Combes, F. 1997, *A&A*, 325, 41  
Bolatto, A. D., Warren, S. R., Leroy, A. K., et al. 2013, *Nature*, 499, 450  
Bregman, J. N. 1980, *ApJ*, 236, 577  
Caldú-Primo, A. & Schruba, A. 2016, *AJ*, 151, 34  
Caldú-Primo, A., Schruba, A., Walter, F., et al. 2015, *AJ*, 149, 76  
Caldú-Primo, A., Schruba, A., Walter, F., et al. 2013, *AJ*, 146, 150  
Chastenot, J., De Looze, I., Relaño, M., et al. 2024, *A&A*, 690, A348  
Cortese, L., Watts, A. B., Sun, J., et al. 2026, arXiv e-prints, arXiv:2602.01612  
Dame, T. M., Hartmann, D., & Thaddeus, P. 2001, *ApJ*, 547, 792  
den Brok, J. S., Bigiel, F., Sliwa, K., et al. 2022, *A&A*, 662, A89  
Di Teodoro, E. M. & Fraternali, F. 2015, *MNRAS*, 451, 3021  
Elliott, R., Fisher, D. B., Mazzilli Ciraulo, B., et al. 2026, arXiv e-prints, arXiv:2601.22500  
Evans, N. J., Kim, J.-G., & Ostriker, E. C. 2022, *ApJ*, 929, L18  
Foyle, K., Rix, H.-W., Walter, F., & Leroy, A. K. 2010, *ApJ*, 725, 534  
Fraternali, F. & Binney, J. J. 2006, *MNRAS*, 366, 449  
García-Burillo, S., Combes, F., Usero, A., et al. 2014, *A&A*, 567, A125  
García-Burillo, S. & Guelin, M. 1995, *A&A*, 299, 657

García-Burillo, S., Guelin, M., Cernicharo, J., & Dahlem, M. 1992, *A&A*, 266, 21  
Greve, T. R., Papadopoulos, P. P., Gao, Y., & Radford, S. J. E. 2009, *ApJ*, 692, 1432  
Heald, G., Józsa, G., Serra, P., et al. 2011, *A&A*, 526, A118  
Howk, J. C. & Savage, B. D. 2000, *AJ*, 119, 644  
Jiao, Q., Zhu, M., Vollmer, B., et al. 2025, *ApJ*, 986, 46  
Kamphuis, P., Peletier, R. F., Dettmar, R.-J., et al. 2007, *A&A*, 468, 951  
Kramer, C., Penalver, J., & Greve, A. 2013, in *Proceedings Title*  
Krause, M., Irwin, J., Wiegert, T., et al. 2018, *A&A*, 611, A72  
Kreckel, K., Blanc, G. A., Schinnerer, E., et al. 2016, *ApJ*, 827, 103  
Li, A., Fraternali, F., Marasco, A., et al. 2023, *MNRAS*, 520, 147  
Li, J.-T., Bregman, J. N., Wang, Q. D., Crain, R. A., & Anderson, M. E. 2018, *ApJ*, 855, L24  
Locatelli, N., Ponti, G., Zheng, X., et al. 2024, *A&A*, 681, A78  
Mac Low, M.-M. & McCray, R. 1988, *ApJ*, 324, 776  
Melioli, C., Brighenti, F., D’Ercole, A., & de Gouveia Dal Pino, E. M. 2008, *MNRAS*, 388, 573  
Mertsch, P. & Vittino, A. 2021, *A&A*, 655, A64  
Nakanishi, H. & Sofue, Y. 2006, *PASJ*, 58, 847  
Oosterloo, T., Fraternali, F., & Sancisi, R. 2007, *AJ*, 134, 1019  
Patra, N. N. 2020, *A&A*, 638, A66  
Pety, J., Schinnerer, E., Leroy, A. K., et al. 2013, *ApJ*, 779, 43  
Querejeta, M., Leroy, A. K., Meidt, S. E., et al. 2024, *A&A*, 687, A293  
Querejeta, M., Schinnerer, E., Meidt, S., et al. 2021, *A&A*, 656, A133  
Rand, R. J. 1997, *ApJ*, 474, 129  
Reach, W. T., Fadda, D., Rand, R. J., & Stacey, G. J. 2025, *Universe*, 11, 127  
Rossa, J. & Dettmar, R.-J. 2003a, *A&A*, 406, 493  
Rossa, J. & Dettmar, R.-J. 2003b, *A&A*, 406, 493  
Roy, A., Nath, B. B., Sharma, P., & Shchekinov, Y. 2016, *MNRAS*, 463, 2296  
Rupen, M. P. 1991, *AJ*, 102, 48  
Sancisi, R. & Allen, R. J. 1979, *A&A*, 74, 73  
Scoville, N. Z., Thakkar, D., Carlstrom, J. E., & Sargent, A. I. 1993, *ApJ*, 404, L59  
Shapiro, P. R. & Field, G. B. 1976, *ApJ*, 205, 762  
Söding, L., Edenhofer, G., Enßlin, T. A., et al. 2025, *A&A*, 693, A139  
Sofue, Y. & Nakai, N. 1993, *PASJ*, 45, 139  
Sommer-Larsen, J. 2006, *ApJ*, 644, L1  
Swaters, R. A., Sancisi, R., & van der Hulst, J. M. 1997, *ApJ*, 491, 140  
Tüllmann, R., Pietsch, W., Rossa, J., Breitschwerdt, D., & Dettmar, R. J. 2006, *A&A*, 448, 43  
Verstappen, J., Fritz, J., Baes, M., et al. 2013, *A&A*, 556, A54  
Voigtländer, P., Kamphuis, P., Marcelin, M., Bomans, D. J., & Dettmar, R.-J. 2013, *A&A*, 554, A133  
Walter, F., Weiss, A., & Scoville, N. 2002, *ApJ*, 580, L21  
Wang, T.-R., Zhu, W., Li, X.-F., Hong, W.-S., & Feng, L.-L. 2026, *MNRAS*, 546, stg128  
Xilouris, K. M., Kramer, M., Jessner, A., et al. 1998, *ApJ*, 501, 286  
Yim, K., Wong, T., Howk, J. C., & van der Hulst, J. M. 2011, *AJ*, 141, 48  
Zschaechner, L. K., Rand, R. J., Heald, G. H., Gentile, G., & Kamphuis, P. 2011, *ApJ*, 740, 35

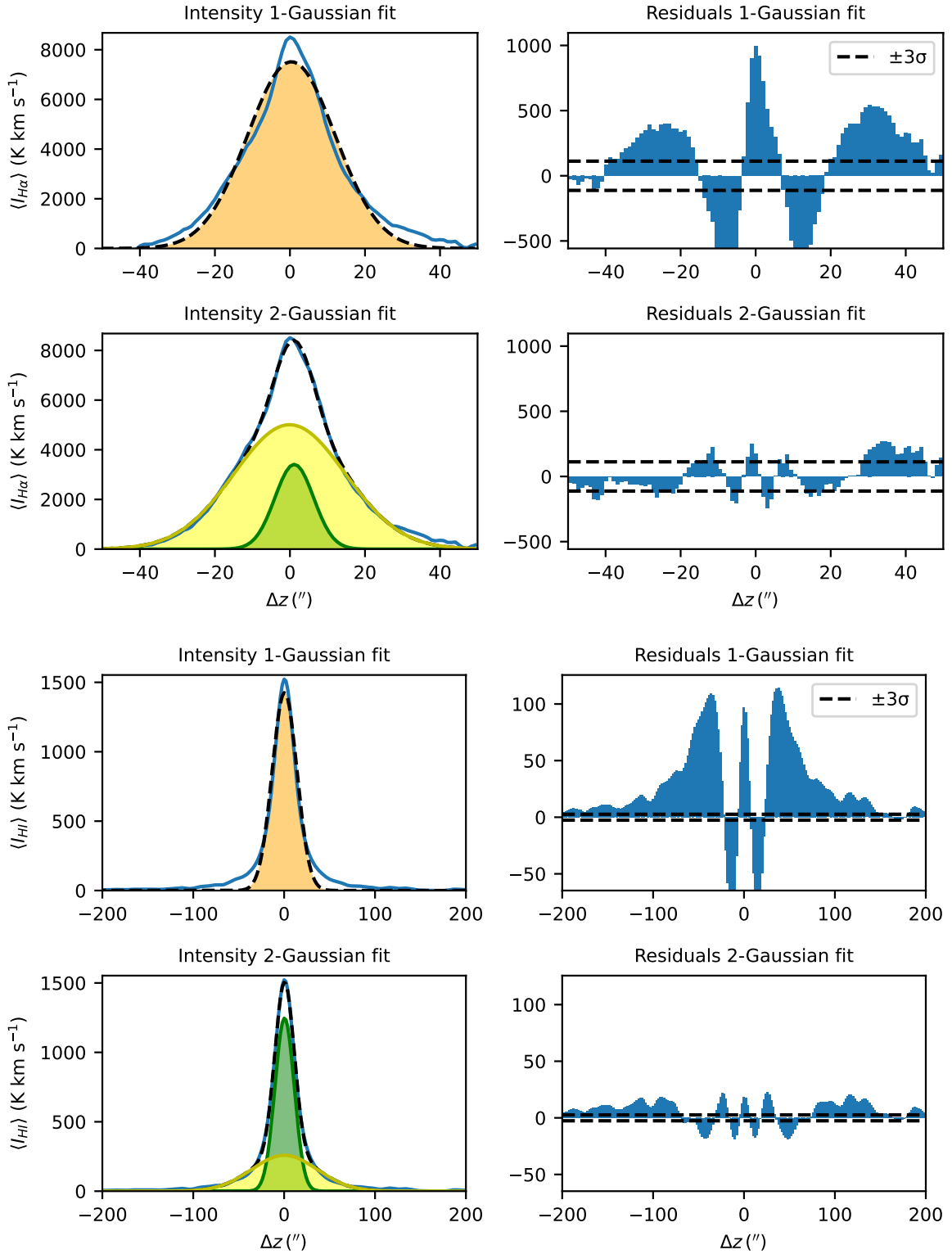
**Appendix A: Channel maps**


**Fig. A.1.** Channel maps of the CO (2-1) intensity of NGC 891, as black contours from  $3\sigma_{\text{ch},\text{CO}}$  to  $600\sigma_{\text{ch},\text{CO}}$  in steps of 0.38 dex, where  $\sigma_{\text{ch},\text{CO}}$  is the rms noise of the channel maps after a  $\Delta v = 50 \text{ km s}^{-1}$  spectral interpolation ( $\sigma_{\text{ch},\text{CO}} = 3.4 \times 10^{-3} \text{ K}$ ). The background image shows the  $\text{H}\alpha$  zeroth-moment map from Kamphuis et al. (2007).

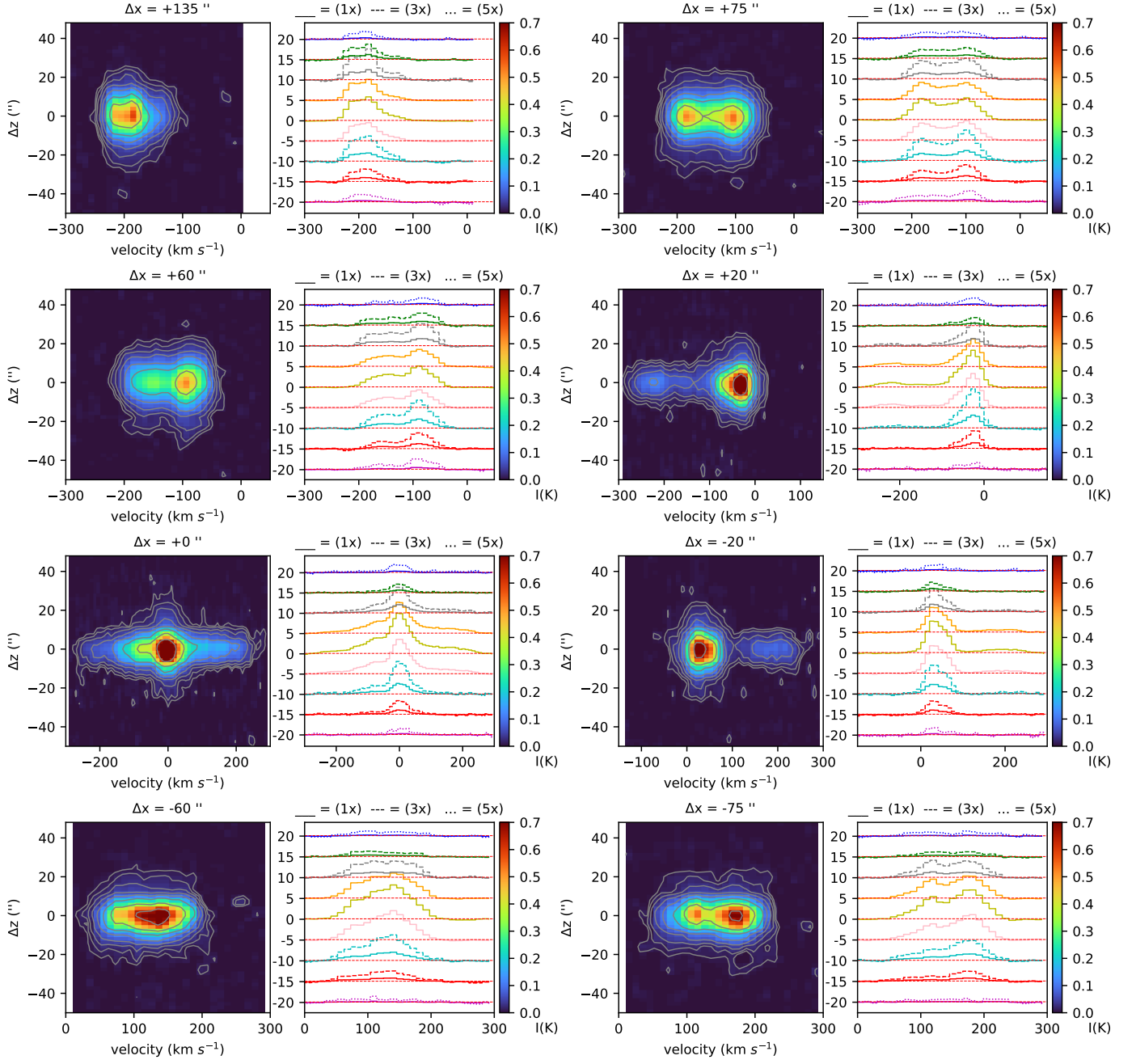


**Fig. A.2.** Channel maps of the CO (2-1) intensity of NGC 891 as black contours, the same as the ones on Figure A.1. The background image shows the USM of the V-band from Howk & Savage (2000).

**Appendix B: Gaussian fits of the integrated intensity and residuals.**



**Fig. B.1.** Same as Figure 5 for HI and H $\alpha$  ( $\sigma_{HI} = 864$  mK,  $\sigma_{H\alpha} = 37$  K).

**Appendix C: PV at different radial slices. Velocity spectra at different heights.**


**Fig. C.1.** Position-velocity slices of CO at different  $\Delta x$ . Grey contours increase logarithmically from  $3\sigma_{\text{ch,CO}}$  to  $600\sigma_{\text{ch,CO}}$  ( $\sigma_{\text{ch,CO}} = 3.5$  mK). On the right side of each map: spectra at different  $\Delta z$  offsets. Each curve has an arbitrary vertical offset, for clarity. Red dotted horizontal line denotes the  $3\sigma_{\text{ch,CO}}$  limit of each curve.

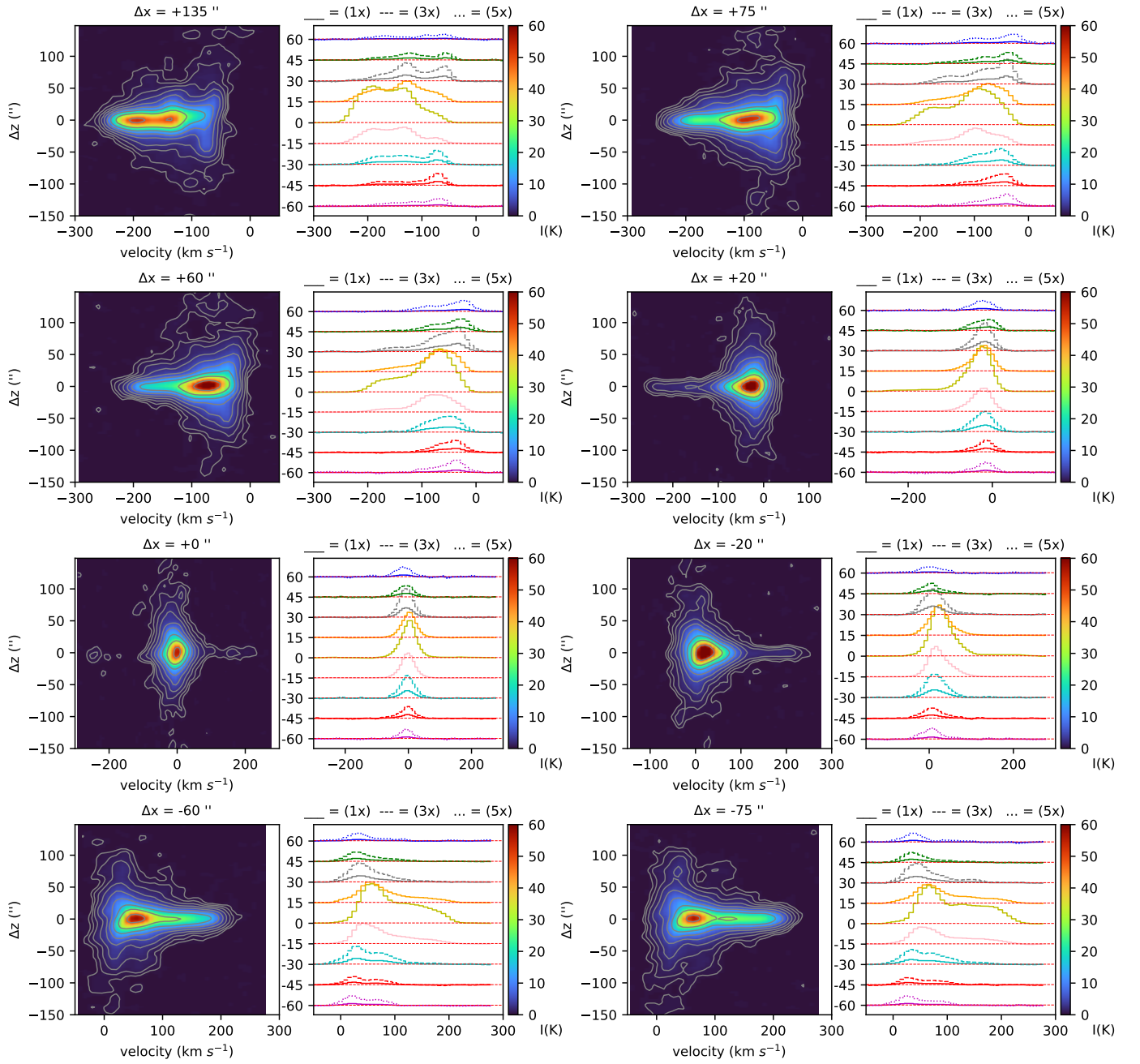


**Fig. C.2.** Same as C.1 for HI ( $\sigma_{\text{ch,HI}} = 147 \text{mK}$ ).

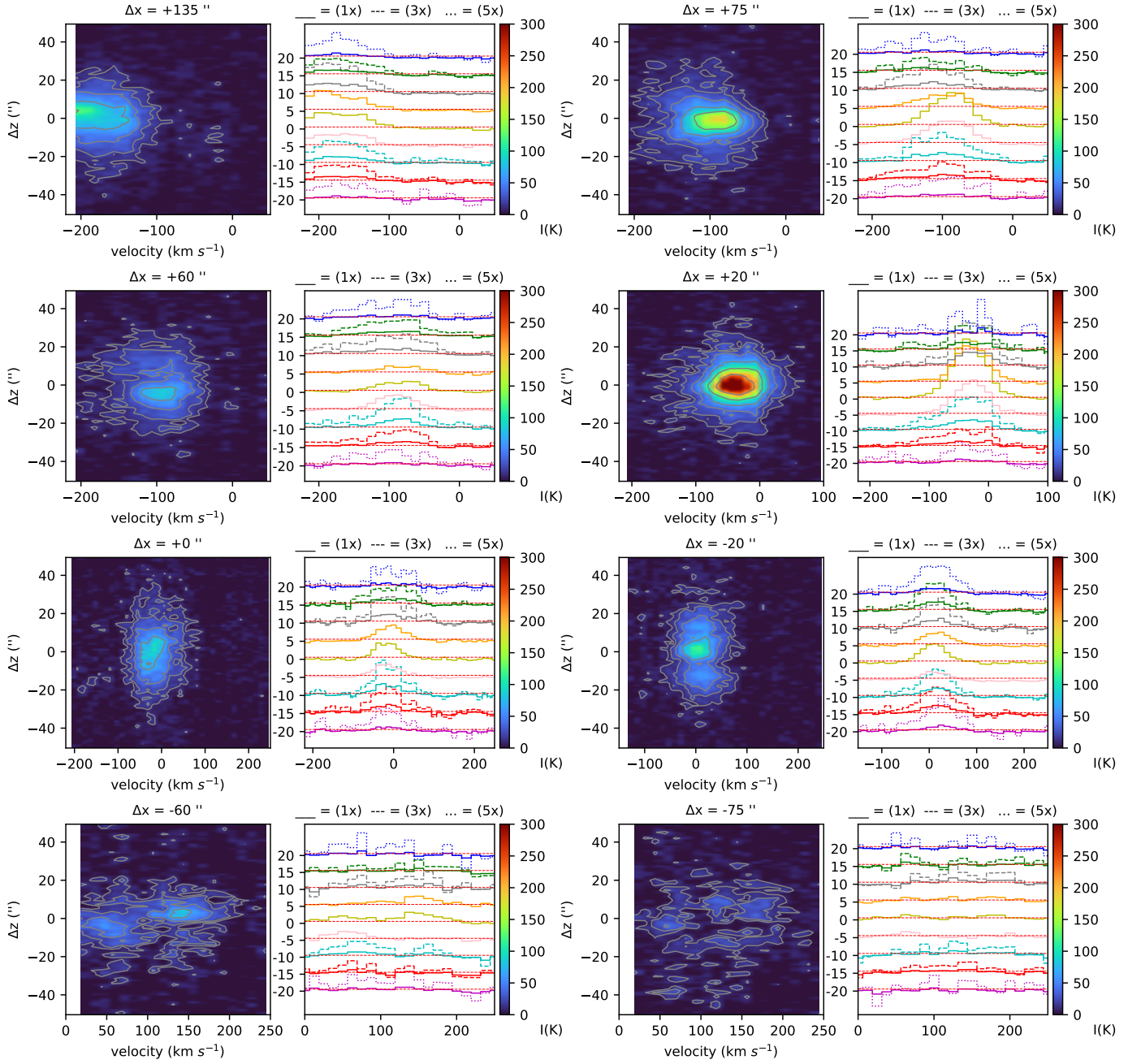


Fig. C.3. Same as C.1 for H $\alpha$  ( $\sigma_{\text{ch,H}\alpha} = 3.8K$ ).